Anisotropic high cycle fatigue property of Sc and Zr-modified Al-Mg alloy fabricated by laser powder bed fusion

Zehao Qin [a,b], Nan Kang [a,b,c,*], Mohamed El Mansori [c], Zihong Wang [a,b], Haoxiang Wang [a,b], Xin Lin [a,b,*], Jing Chen [a,b], Weidong Huang [a,b]

a: State Key Laboratory of Solidification Processing, Northwestern Polytechnical University, Xi'an, Shaanxi, 710072, PR China

b: Key Laboratory of Metal High Performance Additive Manufacturing and Innovative Design, MIIT China, Northwestern Polytechnical University, Xi'an, Shaanxi 710072, PR China

c: Arts et Métiers institute of technology, MSMP, HESAM Universite, F-51006, Chalons en Champagne, France

**corresponding authors*

State Key Laboratory of Solidification Processing,

Northwestern Polytechnical University,

Xi'an Shaanxi 710072, PR China

E-mail address: nan.kang@nwpu.edu.cn (N. Kang).

xlin@nwpu.edu.cn (X. Lin)

OCRID: 0000-0002-4998-5600(N. KANG)

Nomenclature

Symbols		**Abbreviations**	
YS	Yield strength	2D	Two-dimensional
UTS	Ultimate strength	3D	Three-dimensional
ε_f	Elongation to failure	LAM	Laser additive manufacturing
E	Young's modulus	LPBF	Laser powder bed fusion
UT	Deformation energy	LDED	Laser direct energy deposition
σ_e	effective stress amplitude	EG	Equiaxed grain
σ_f	Fatigue strength	UFG	Ultrafine grain
σ_{max}	maximum stress	LD	Loading direction
R	Stress ratio	PD	Parallel direction
σ_a	Stress amplitude	TD	Transverse direction
F_w	Geometric factor	BD	Building direction
√area	Murakami's parameter	SEM	Scanning electron microscopy
ΔK	Stress intensity factor range	XRT	X-ray tomography
$\cos(\alpha)\cos(\beta)$	Schmid factor	TEM	Tansmission electron microscopy
K-T	Kitagawa-Takahashi	FIB	Focus ion beam
V/S	Volume/Surface area	BSE	Backscatter electron
d	Equivalent diameter	FCC	Face-centered cubic
σ_e	effective stress amplitude	MUD	Multiple uniform density
ΔK_{th}	Crack growth threshold	APB	Antiphase boundary
		SRO	Short-range order

Abstract

This work investigates the defects (pore and lack of fusion), microstructure, and fatigue properties of Sc and Zr-modified Al–Mg alloy on different building directions fabricated by laser powder bed fusion (LPBF). The results showed that transversely deposited (TD) samples exhibited a superior fatigue strength (100.5 MPa) compared to that (57 MPa) of the parallelly deposited (PD) sample, while their tensile and hardness properties were similar. This phenomenon is attributed to two factors: defects and grain/microstructure. For the defects, the lack of fusion resulted in a higher stress concentration in the PD samples than that of the TD samples in the crack initiation stage. For the microstructure, owing to the significant cyclic softening and indistinctive crack deflection of the columnar grains, they became soft with the decrease in fatigue resistance. The different crack propagation directions led to different columnar grain/equiaxed grain area ratios for the anisotropic fatigue properties. Furthermore, in the TD samples, some grains, with the < 110 > || building direction orientation, partly led to a higher fatigue resistance of the TD sample than of the PD sample owing to the exceptional dislocation formation.

Keywords: Al–Mg–Sc–Zr alloy; Selective laser melting; High cycle fatigue; Anisotropy.

1. Introduction

Laser additive manufacturing (LAM) is a series of technologies with one basic principle for fabrication of complex high-performance components by adding a material layer by layer. Based on the feeding system [1,2], LAM can be divided into two major categories: (i) laser directed energy deposition (LDED), in which synchronous powder serves as the feeding system; (ii) laser powder bed fusion (LPBF), which based on a powder bed. These manufacturing techniques can realize the 1:1 transformation of a digital model to solid parts through the fixed-point interaction of the laser-induced heat source and powder depending on the digital path objected by a computer [1,3–5]. In addition, the combination of laser-induced heat flux and relatively high travel speed can induce localized transient temperature responses and extremely high temperature gradient (~10^3 – 10^7 K/m) in the melt pool, which provides LAM-fabricated parts with nonequilibrium solidification microstructures and excellent mechanical properties [3,6–8].

However, conventional high-strength aluminum alloys, such as 2xxx (Al–Cu), 6xxx (Al–Mg–Si), and 7xxx (Al–Zn–Mg–Cu), have wide freezing temperature intervals and thus are ill-suited to accommodate the rapid solidification characteristics of the LAM technology, wherein high hot-tearing susceptibilities commonly exist and are difficult to eliminate [7,9–12]. As a result, the majority of previous studies on LAM-fabricated Al alloys are based on eutectic or near-eutectic Al–Si casting alloys. Although they have good hot-cracking resistances, their weak mechanical properties restrict their further industrial application of structural relevance [6,13–16]. Hence,

the development of high-strength aluminum alloys specifically tailored for LAM attracts increasing attention [15,17–21].

Recently, the addition of Sc/Zr elements has been demonstrated as a feasible modification method for LAM-fabricated Al alloys [9–11,18,21]. The main modification roles of Sc/Zr can be explained as follows: (i) The coherent Al_3(Sc/Zr) precipitates formed during solidification can provide in-situ heterogeneous nucleation sites for α-Al crystallization due to the low lattice misfit with the matrix, forming finer equiaxed grains rather than coarsen columnar grains with epitaxial growth characteristics. The formation of such refined equiaxed grains (EGs) not only solves the problem of thermal cracking by eliminating long intergranular liquid channels between long columnar grains (CGs), but also provides isotropic and improved static mechanical properties; (ii) These Sc/Zr-modified alloys can be further strengthened and promote thermal stability by precipitation of secondary Al_3(Sc/Zr) particles through direct aging [22]; (iii) The unique heterogeneous microstructure, composed of an EG band and CG domain within one molten pool, is a common feature of these alloys and exhibits a superior combination of strength and ductility to those of their homogeneous counterparts [17,23–25]. During plastic deformation, the gradient strain distribution at the interface of two grain regions produces geometrically necessary dislocations, resulting in an additional back-stress hardening (more accurately referred to as hetero-deformation-induced hardening) and thus a higher strain-hardening ability [26].

The literature on the mechanical properties of Sc/Zr-modified Al alloys

manufactured by LAM was summarized in Table 1[9–11,18,21,22,27–33]. These alloys not only maintain strength–ductility synergy but also exhibit low anisotropies in static mechanical properties owing to the effects of the Sc/Zr modification. In addition, the addition of Sc/Zr elements provides a viable method for in-situ modification of microstructure and properties. For LDED, Wang et al. [33] reported that the transition of microstructure from an equiaxed grain structure to a bi-modal grain structure can be adjusted by controlling the substrate cooling conditions. Kürnsteiner et al. [34] also showed the potential of making use of the intrinsic heat treatment to change the size and number of precipitates. For LPBF, preheating [35,36], process parameters [35,37], and rescanning [38] can in-situ alter the grain evolution behavior, thus changing the volume fraction of both grains. Moreover, the high cooling rate of LPBF is favorable for the formation and refinement of bi-modal grain structure and high strength [17,27].

Currently, many studies, performed on LPBF-fabricated Al alloys, turned to investigate their fatigue behaviors. Most of them focused on Al-Si series alloys. These studies [16,39,40] showed that the fine cellular microstructure brings beneficial effects and improved fatigue properties could be achieved by heat treatment. But defects such as pores and lack of fusion led to deteriorated and anisotropic fatigue behavior. Xu et al. [41] investigated the effects of building direction on fatigue behavior of the LPBF-fabricated AlSi10Mg alloy. The 0° samples show a higher fatigue strength than the 45° and 90° samples because of the smaller defect size distribution of the 0° sample. Wu et al. [42] also reported the low fatigue strength,

when the loading direction was parallel to the build direction, was attributed to the larger size of the projected area of LoF defects vertical to the building direction than that along building direction.

However, it is still unclear that how the metastable metallurgical features of the LPBF process, especially the rapid solidification, induced defects, heterogeneous grain structure, and precipitates, influence the fatigue properties of the LPBF-fabricated Sc/Zr modified Al alloys due to their different metallurgical behavior and heterogeneous structure from Al-Si alloys. On the other hand, the special layer by layer manufacturing procedure will bring new challenges for understanding the metallurgical behavior with emphasis on the building direction. Therefore, this study aims to clarify the effects of multi-scale features on the fatigue properties of LAM-fabricated Sc/Zr-modified Al alloys, which is important for the design and application.

In this paper, we introduce Sc/Zr-modified Al alloy specifically tailored for the LPBF, Al–Mg–Sc–Zr alloy, to investigate the effects of Sc/Zr-modified heterogeneous structure characteristics on high-cycle fatigue performances in different deposition directions. The multi-scale heterogeneous structure of the LPBF-fabricated Al–Mg–Sc–Zr alloy was comprehensively characterized, including defects, grain structures, and precipitation phases. Based on the characterization, the effects of these factors on the fatigue crack initiation and propagation were analyzed and their respective mechanisms under dynamic loading conditions were obtained. This study can contribute to the further development of LPBF-fabricated aluminum alloys with

isotropic and integrated (monotonic-dynamic) mechanical performances.

Table 1 Literature review on tensile performance of Sc/Zr-modified Al alloys fabricated by LAM (TD represents deposition direction is transverse to loading direction and PD is parallel to loading direction).

Refs.	Material	Yield strength (MPa)	UTS (MPa)	ε_f (%)	Heat treatment	Orientation	Process
[43]	Al–Mg–Sc–Zr	453 ± 20	530 ± 12	9 - 10	Aging	TD	LPBF
		450 ± 9	515 ± 16	9 - 10		PD	LPBF
[29]	Al–Mg–Sc–Zr	510 ± 2	531 ± 2	15.0 ± 0.3	Aging	TD	LPBF
[44]	AA5083 + Zr	309 - 325	380 - 399	13.9 – 14.5	Aging	-	LPBF
[30,31]	AlZnMgScZr	418 ± 3	436 ± 3	11 ± 1	T6	-	LPBF
[18]	Al–Mg–Si–Sc–Zr	-	506 - 550	8-17	Aging	-	LPBF
[21]	Al–Mn–Sc	556 ± 11	-	18±1.6	Aging	TD	LPBF
		530 - 550	-	12-14		PD	LPBF
[22]	Al–Mg–Zr	349 ± 15	383 ± 5	19.5 ± 4.4	Aging	PD	LPBF
		365 ± 11	389 ± 4	23.9 ± 4.4		TD	LPBF

			621				
[9]	7075 + Sc and Zr	-	(Compressive strength)	-	As-built	-	LPBF
[10]	AA6061 + Zr	299.8	327.3	13.9	T6	TD	LPBF
[11]	Al–Cu–Mg–Zr	446 ± 4.3	451 ± 3.6	2.7 ± 1.1	As-built	-	LPBF
[32]	Al–Cu–Si–Sc–Zr	236	329	9.7	As-built	TD	LPBF
[33]	Al–Mg–Sc–Zr	261 ± 1	384 ± 6	20.2 ± 1.3	Aging	TD	LDED + Water cooling
[27]	Al–Mg–Sc–Zr	192	280	5.9	-	TD	LDED

2. Materials and methods

2.1.Powder and sample preparation

A commercially available Al–Mg–Sc–Zr powder, fabricated using a vacuum induction gas atomization process, was used in this study. The chemical compositions of the experimental powder were measured by inductively coupled plasma atomic emission spectrometry according to the American Society for Testing and Materials (ASTM) E3061-17 standard [45], as shown in Table 2. The particle morphology and size distribution of the as-received powder are shown in Fig. 1(a). Most of the powder is spherical. The satellite powder is located at the surface of the larger powder. The D10, D50, and D90 values, which indicate the maximum particle diameters that include 10%, 50%, and 90% of the particles (volume-weighted basis), were determined to be 12.2, 26.0, and 46.8 μm, respectively. All powders were dried under

vacuum for 3 h at 120 °C prior to the sample fabrication. 10 × 10 × 10 mm^3 cubic samples, a total of 18 pieces, were fabricated for process parameter optimization (e.g., laser power and scanning speed). The relative densities of the samples were confirmed by the Archimedes method and statistical results of the area of defects using the optical microscope, as shown in the supplement (Fig. S1 and S2). A strip scan strategy with the scanning direction rotation of 67° between the consecutive layers, 80℃ of platform temperature, and an Ar atmosphere with an O concentration below 200 ppm were used. A relative density of ~99.4% was realized using the optimized parameters and remained constant during the fabrication of all samples in this study, as summarized in Table 3.

Table 2 The chemical compositions of the experimental powder (wt.%).

Si	Mg	Mn	Fe	Sc	Zr	Al
0.09	4.74	0.47	0.10	0.70	0.32	Bal.

Table 3 Constant process parameters for LPBF-fabricated Al–Mg–Sc–Zr alloy.

Process parameter	Laser power (W)	Scanning speed (mm/s)	Layer thickness (μm)	Hatch space (mm)
Value	370	1000	30	0.12

A commercial EOS M280 machine, with a laser beam diameter of 100 μm, was used to deposit two groups of Al–Mg–Sc–Zr samples in the cylindrical form. One of them contains a series of cylindrical rods whose deposition direction is parallel (PD)

to the loading direction (LD), while the other contains cylindrical rods whose deposition direction is transverse (TD) to the LD, as shown in Fig. 1(b). The as-deposited samples were post treated by direct aging in a vacuum furnace before the subsequent machining. The direct aging treatment was carried out at 325 ℃ for 4 h, which ensures the maximum tensile strength of the LPBF-fabricated Al–Mg–Sc–Zr alloy, as reported by Wang et al. [29]. Both TD and PD cylindrical rod groups included fatigue specimens and tensile specimens with a nominal height of ~108 mm and diameter of ~20 mm and nominal height of ~67 mm and diameter of ~11 mm, respectively, at least to leave the machining allowance of 2 mm. After heat treatment, fatigue specimens and tensile specimens in accordance with GB/T 3075-2008 [46] and GB/T 228.1-2010 [47], as shown in Fig. 1(c), were obtained by machining work. Then, all specimens were polished by the numerical control machine tool (K6530) using abrasive paper (2000 #), to achieve a uniform and high surface roughness (Ra < 0.4 μm). Therefore, the effect of surface roughness on the fatigue properties can be ignored.

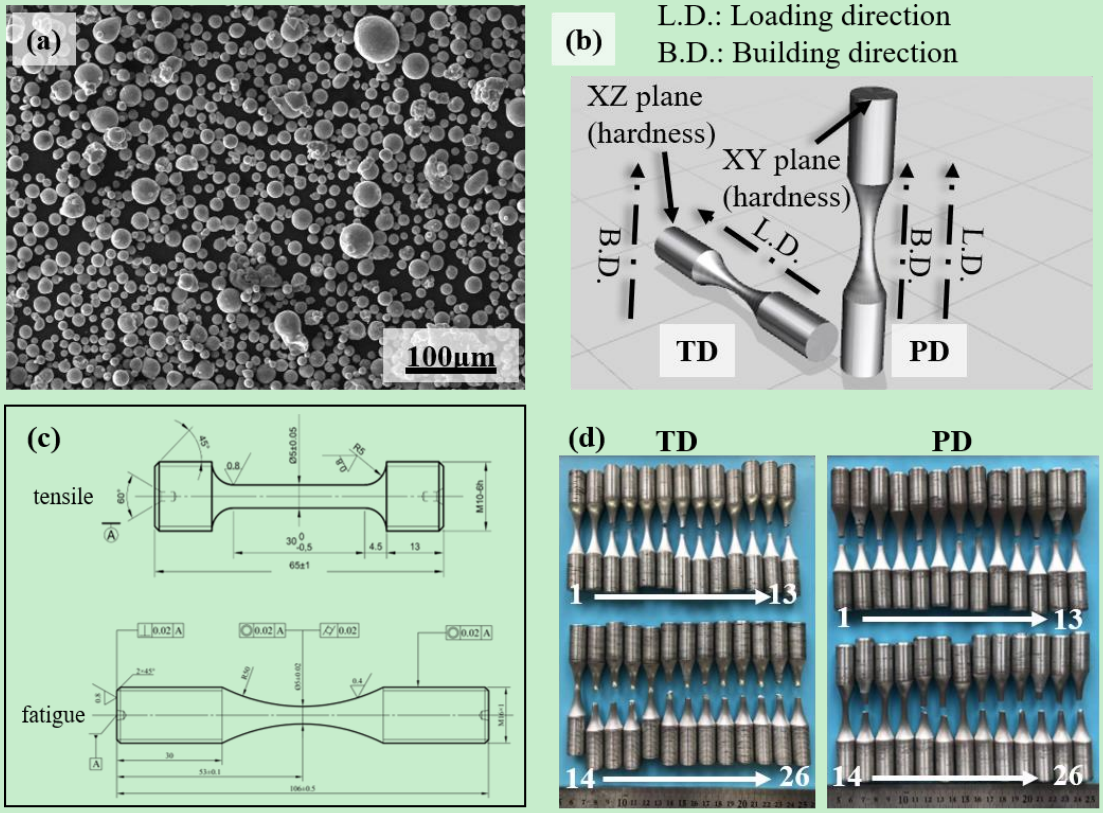

Fig. 1. (a) Secondary electron image and particle size distribution (the inset) of Al–Mg–Sc–Zr powder. (b) Schematic of fatigue specimens in the TD (left), PD (right), and location of XY and XZ plane. (c) Drawings of tensile and fatigue specimens. (d) Fatigue specimens of LPBF-fabricated Al–Mg–Sc–Zr alloy, left is TD and right is PD.

2.2.Mechanical properties

The machined and polished tensile specimens under the aging conditions with a gauge length of 30 mm and diameter of 5 mm were used to carry out room-temperature uniaxial tensile tests using an Instron 3382 universal testing machine. The nominal crosshead displacement rate was 1 mm/min. The tensile properties were averaged by three measurements. To distinguish the differences in the mechanical

properties of the EG bands and CG domains under aging conditions, the microhardness was measured using an LM248AT Vickers hardness tester (LECO) with a load of 5 g and holding time of 15 s.

Stress-controlled fatigue tests were conducted at room temperature using an MTS Landmark 200-Hz machine under various stress amplitudes. The stress ratio (R) of the tests was 0.1, while the waveform was sinusoidal with a nominal frequency of 100 Hz. The whole process of testing was based on the Chinese standard GB/T 3075-2008 “Metal Material Axial Loading Fatigue Test Method” [46]. The fatigue tests were stopped at specimens that were completely fractured (failed) or loaded for 10^7 cycles (passed). Subsequently, the fracture surfaces of the failed samples were evaluated using scanning electron microscopy (SEM) to investigate the fracture characteristics.

2.3.Characterization

After the fatigue tests, the defect population in the fatigue gauge section of the passed specimens was characterized using X-ray tomography (XRT) using a Zeiss Xradia 520 versa machine. To ensure penetration, a voltage of 120 kV and current of 120 μA were used. The data were collected with a voxel size of 2.51 μm. The two-dimensional (2D) projection images were reconstructed into three-dimensional (3D) topography using the DRAGONFLY software.

Before the microstructural characterization, the as-deposited samples were sectioned parallel and transverse to the deposition direction, mechanically ground, and then polished using 600-to 5000-grit SiC papers and 0.25-μm colloidal silica

suspension, respectively. The surfaces of the polished specimens were etched with the Keller's reagent (HF:HCl:HNO_3:water = 1:1.5:2.5:95) to observe the macrostructure using a GX71 OLYMPUS optical microscope and electropolished at a voltage of 23 V for 10 s with an electrolyte (10 vol.% perchloric acid in a 90-vol.% ethanol solution) using a Struers electrolytic instrument (LectroPol-5) for the observation of the microstructure through an electron back-scatter diffraction (EBSD) test using a FEI Helios Nano-Lab SEM machine with a scanning step size of 0.2 μm. Data were analyzed using the CHANNEL5 software package.

To observe the phase distribution and the dislocation configurations of the fatigue-failed sample through a transmission electron microscopy (TEM) system (double C_s corrector), two methods of preparing thin foils for TEM observation were employed. One of them was cut from the as-deposited sample and ground to a thickness of 50 μm using a 1500-grid SiC paper, and then a φ3-mm foil was prepared via twin jet electrolytic thinning. The other was extracted from the longitudinal plane of the fatigue-failed specimen (the direction of the plane is parallel to the deposition direction, while the extraction location is near the fracture surface) in the TD and PD using an FEI Helios Nano-Lab G4 CX FIB, as shown in Fig. 2. Sizes of approximately 4 × 6 × 0.8 μm^3 (height × width × thickness) of the foil were obtained by milling using a focused beam of Ga^+ ions at a voltage of 30 kV and currents of 65, 9.3, and 0.23 nA. Before the focused ion beam (FIB) sample fabrication, the crystallographic orientations of these regions were analyzed by EBSD. The nanoscale precipitates were also analyzed by the TEM on an electrolytic foil in the aged

samples.

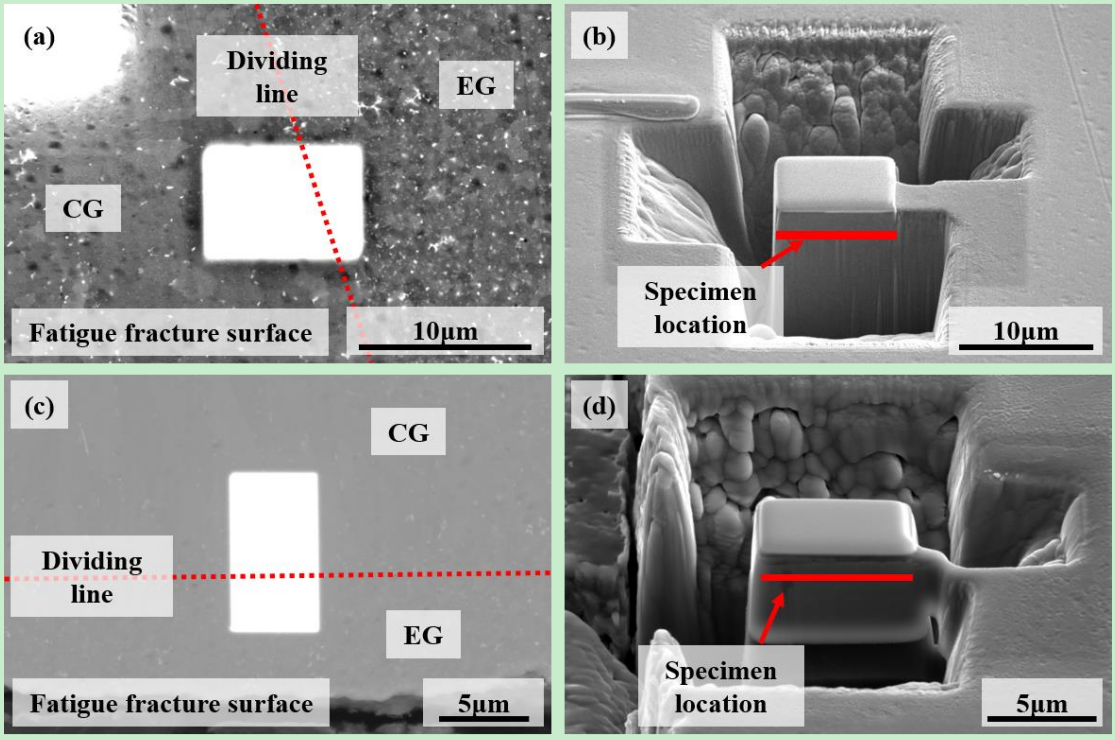

Fig. 2. Schematic diagrams of positioning and extracting a TEM thin foil from longitudinal section of a failed specimen using Focus ion beam (FIB) technique (a, b) TD; (c, d) PD.

3. Results

3.1 Microstructure analysis

3.1.1 Defect distribution

Considering the different aspect ratios of the specimens and building times resulting from different building directions, the defects might be diverse [42,48–50]. The defect characteristics of the LPBF-fabricated Al–Mg–Sc–Zr alloy in the TD and PD were analyzed by XRT. The densities of the samples in the TD and PD estimated by XRT were 99.52% and 99.43%, respectively, which mainly ascribed to more defects in the PD than those for the TD. The longer interval time and the bigger

contact area with the substrate of the TD group, compared to the PD group, can increase the cooling rate of the molten pool [51]. So, the TD specimen possesses less defects than the PD specimen. The representative spatial distributions of defects in the TD and PD are presented in Fig. 3a and b. Two types of defects with distinct geometric features were identified (insets of Fig. 3a2 and b2). One of them consists of random high-density small spherical defects. These spherical defects were defined as gas pores with smooth edges. The other with a low density, large size, and irregularity is defined as lack of fusing (LoF). The LPBF-fabricated components always contain pores and LoF defects owing to the uncontrollable gas volatilization and improper process parameters. The volatile gas or protective atmosphere trapped in the molten pool forms pores [52]. The unrealized metallurgical bonding was caused by the insufficient heat input and following liquid metal cooled too quickly to fill this gap result in LoFs [50,53].

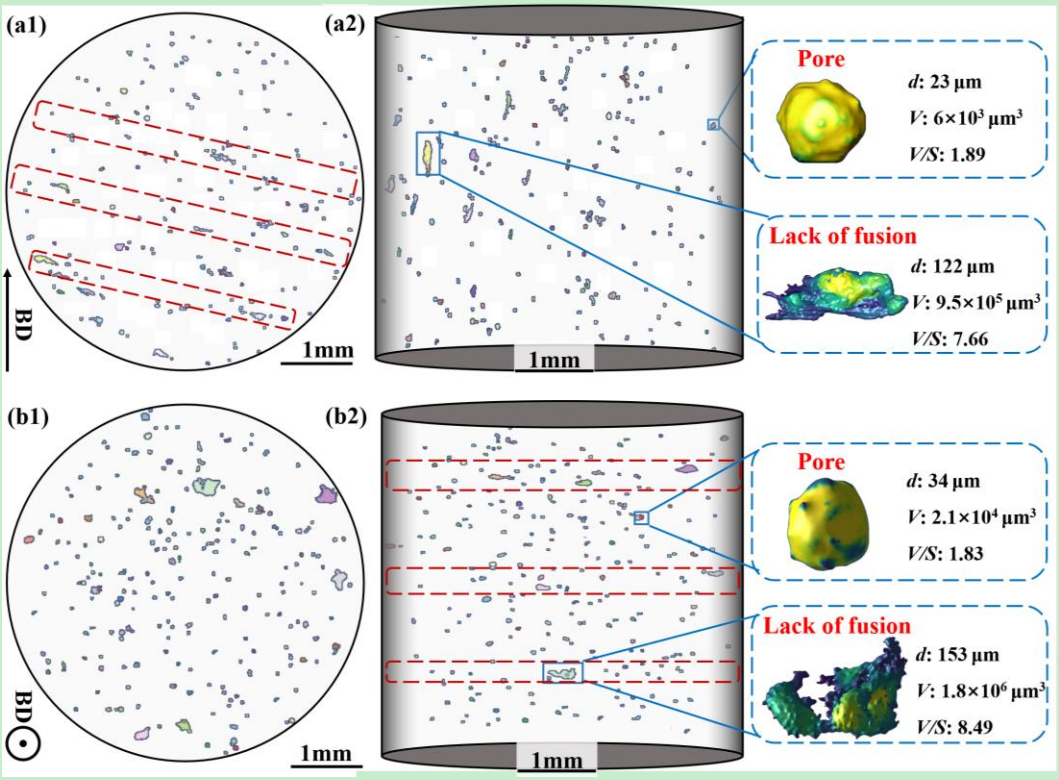

Fig. 3. Reconstructed X-ray tomographic images of specimen of Al–Mg–Sc–Zr showing defect distribution in (a) TD and (b) PD, a1 and b1 are the views from top, a2 and b2 are the views from side.

Fig. 4 shows the features (size, volume/surface area, and defects orientation) of defects in the TD and PD specimens. The equivalent diameter (d) is the spherical diameter with the same volume as the defects. The volume/surface area (V/S) represents the shape of defects with a higher value meaning more irregular. The Φ and θ, respectively, denote the angle between the longest axis and the Z axis, which is parallel to their building direction, and the Y axis, which is vertical to their building direction. The size distributions of defects show a similar trend in the TD and PD specimens with the equivalent diameters of most defects being below 60 μm (Fig. 4a), and their shape tends to be regular (Fig. 4b), which mean the pores dominate the

population. For the defects (LoFs) with big size (> 60 μm), there is a trend for these defects to be irregular (V/S > 4). So, they are few but are dangerous. A connection between the defects orientation and building direction was found from Fig. 4c, the LoFs prefer to $\Phi = 0°$ for the TD specimen and $\Phi = 90°$ for the PD specimen. However, θ randomly distributes from -180° to 180° in both TD and PD specimens. This phenomenon is mainly because the parts are deposited layer by layer (Fig. 4) and the thermal history between adjacent layers exhibits larger fluctuations [49,54,55], and the 67° rotation angle can effectively dislocate the orientation of defects at each layer.

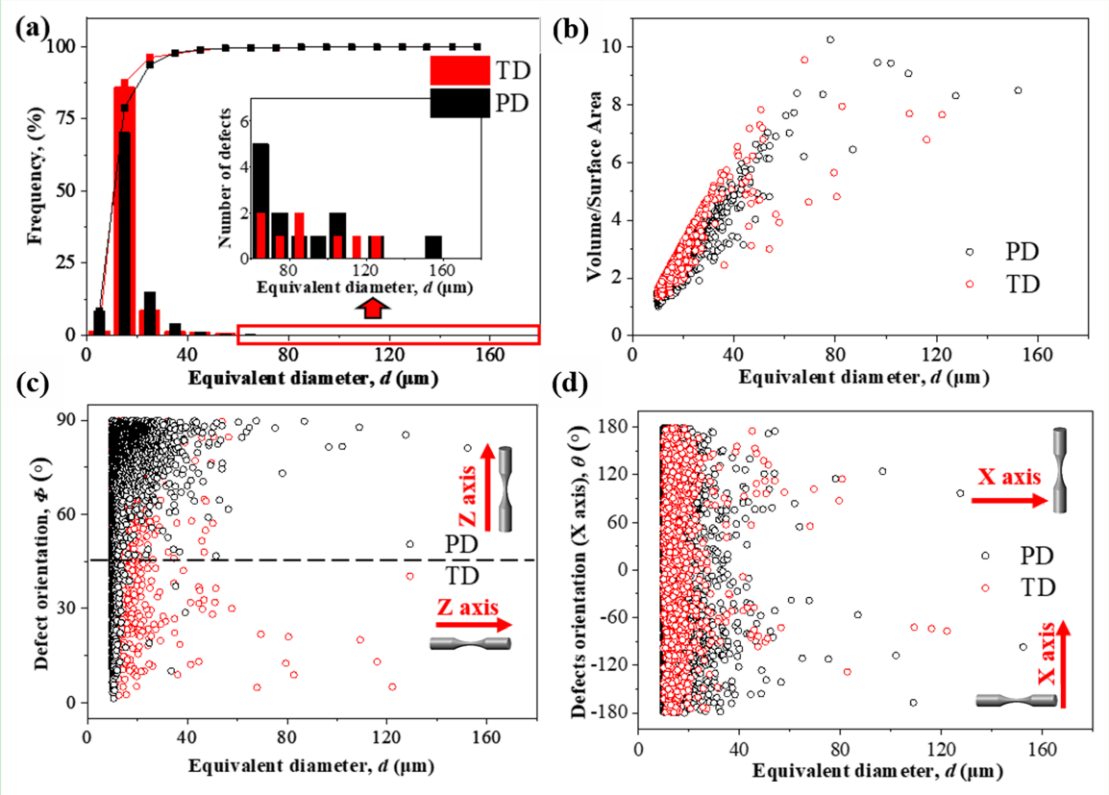

Fig. 4 Defects features statistics of TD and PD specimens. (a) Size distribution. (b) Distribution of equivalent diameter and the volume/surface area of defects. (c) and (d) defects orientation distribution correlated to the Z axis, which is parallel to their

loading direction and the X axis, which is vertical to their building direction, respectively.

3.1.2 Bimodal grain structure

Fig. 5 shows the macro- and microstructures of the LPBF-fabricated Al–Mg–Sc–Zr specimen. Fig. 5a shows a 3D optical macrodiagram of the specimen under aging conditions, with the laser scanning tracks with a rotation angle of 67°, owing to the track-by-track scanning, on the top surface (XY plane) and fish-scale molten pool, owing to the layer-by-layer accumulation, on the side surface (XZ plane). Fig. 5b and c show microimages in the XY and XZ planes, respectively, obtained by backscatter electrons (BSEs). A heterogeneous grain structure, which comprises fine EG bands at the molten pool boundary and elongated CG domains in the center of the molten pool, is formed in the sample. Fig. 5b and c show a large number of white particles, which are mainly Al_3(Sc, Zr) and Al–Mg oxides [22,56], distributed mainly in the EG region and limitedly formed in the CG region. These Al_3(Sc, Zr) precipitations are formed during the solidification of the molten pool. Their lattice structure ($L1_2$) is similar to α-Al (face-centered cubic (FCC)) [57]. Thus, the precipitation behavior of Al_3(Sc, Zr) during solidification is well correlated to the grain morphology [33]. This heterogeneous or bimodal grain structure characteristic of the Al–Mg–Sc–Zr alloy is also consistent with the observations by Spierings et al. [56].

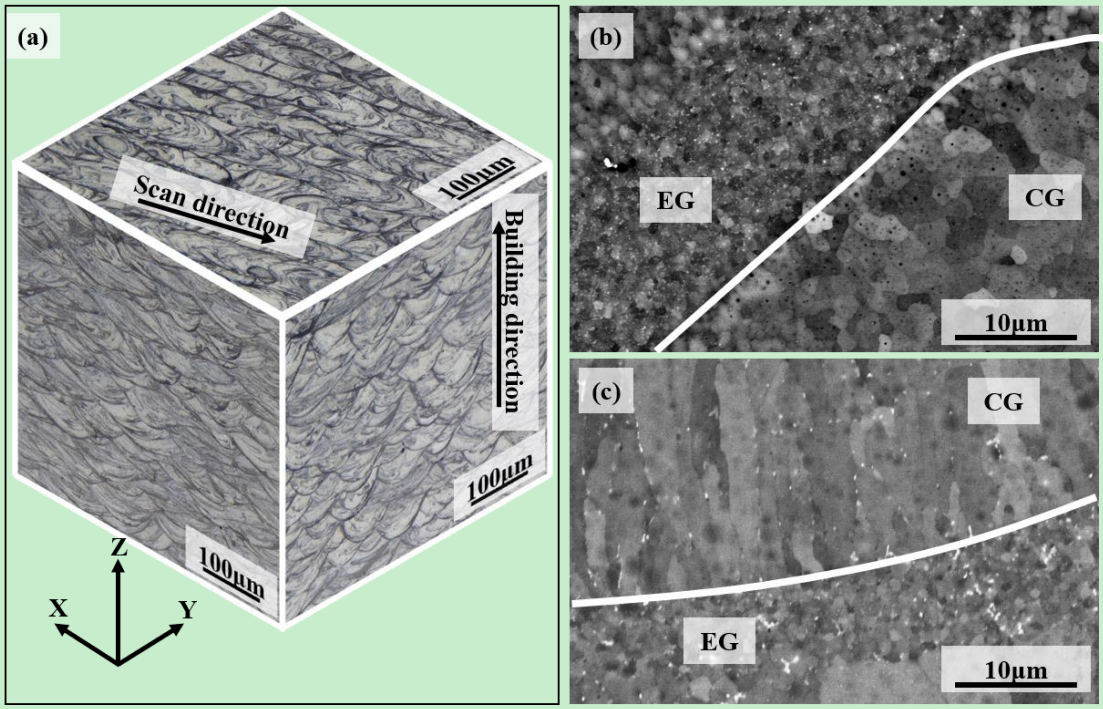

Fig. 5. (a) 3D light optical image of LPBF-fabricated Al–Mg–Sc–Zr alloy. The red line presenting the molten pool boundary. Backscatter electron (BSE) images showing microimages at the melt pool boundary in (b) XY plane and (c) XZ plane.

The inverse polar figure (IPF) maps of the LPBF-fabricated Al–Mg–Sc–Zr alloy at the XY and XZ planes obtained by EBSD are presented in Fig. 6a and b, respectively. A distinct bimodal grain morphology with massive and fine EGs wrapped around CGs is formed in the XZ plane (Fig. 6b). The polar figure of the entire plane is presented in Fig. 6d, without obvious texture (Multiple uniform density (MUD): 3.33) owing to the massive random distribution orientation of EGs. The XY plane exhibits smaller grain size and morphological differences and lower texture strength (MUD: 2.02) (Fig. 6a and c). However, when only the CG region is considered, a stronger solidification fiber texture is formed (Fig. 6a and b). Therefore, the low MUD of the XY plane is mostly attributed to the more visible fraction of

disordered EGs. The average grain sizes on the XY and XZ planes are determined to be 0.93 ± 0.79 and 1.06 ± 0.59 μm, respectively (Fig. 6e and f). As the equivalent grain size (the spherical diameter with the same volume as that of the grains) is counted, the average grain size counted by XY is lower because the XY plane is counted for the cross section of a columnar crystal, which has a smaller area.

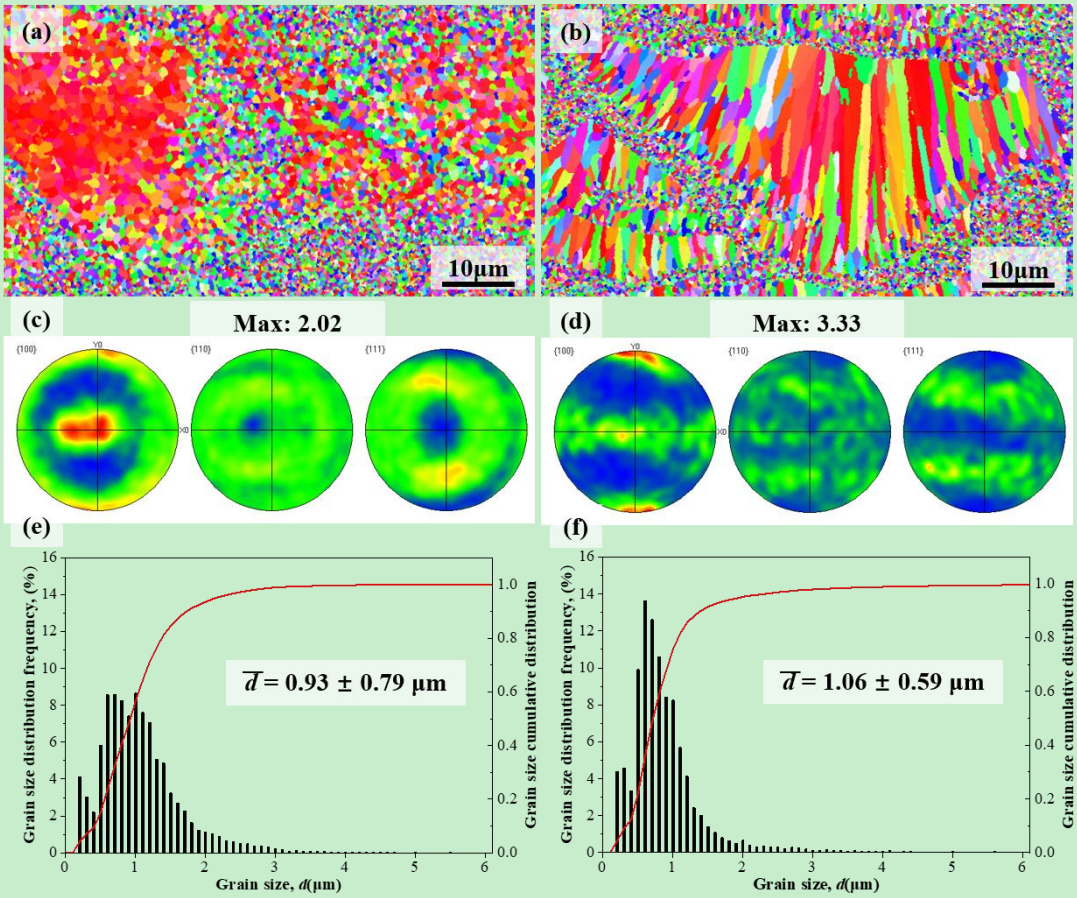

Fig. 6. EBSD maps showing the heterogeneous grain structure, pole figure and grain size distribution of LPBF-fabricated Al–Mg–Sc–Zr alloy in XY plane (a, c and e) and XZ plane (b, d and f).

3.1.3 Precipitation phase

As shown in Fig. 5b and c, numerous precipitates were formed among the Al

matrix. To provide insights into the main precipitates in the Al–Mg–Sc–Zr alloy, high-resolution (HR) TEM images of these precipitates in the EG and CG regions and corresponding selected-area electron diffraction (SAED) patterns along the [001] zone axis are shown in Fig. 7. As shown in Fig. 7a, a bean-shaped particle with a size of 30–40 nm existed in the EG. The 001-type superlattice reflection was apparent based on the SAED pattern. This particle is considered to be primary Al_3(Sc, Zr), which is formed during solidification [29]. Moreover, the HRTEM image obtained from the CGs (Fig. 7d) shows that some particles were embedded in the α-Al matrix. The corresponding SAED patterns demonstrate their $L1_2$ ordered structure and {100} crystal planar space compatible with the α-Al matrix, which indicates their coherency with the α-Al matrix. Owing to the different precipitation kinetics, their sizes vary. The primary Al_3(Sc, Zr) has a larger dimension with a diameter of tens of nanometers, which is a few nanometers for the secondary Al_3(Sc, Zr). Thus, these particles are defined as secondary Al_3(Sc, Zr) formed during the aging process [56].

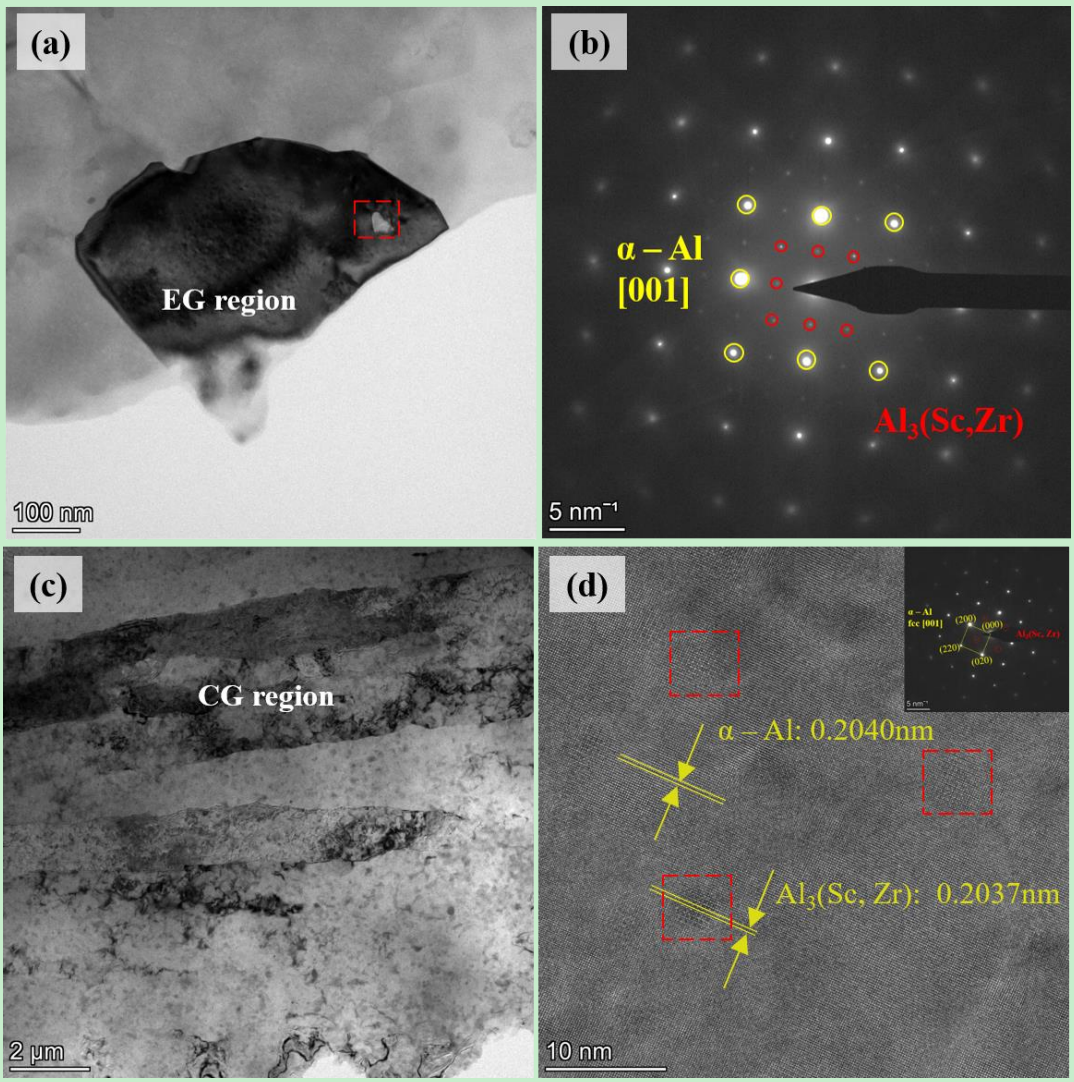

Fig. 7. Bright field (BF) images showing EG (a) and CG (c) regions of Al–Mg–Sc–Zr alloy. (b) SAED image of α-Al and primary Al_3(Sc, Zr). (b) HRTEM image and SAED image (the inset) of secondary Al_3(Sc, Zr).

The particle distributions were further confirmed by scanning TEM–energy-dispersive spectroscopy (STEM-EDS) maps of EG and CG regions, as shown in Fig. 8a and b. Mn/Fe-rich and Mg/Si-rich particles are beset at the grain boundary in both EG and CG regions distributed similarly while Sc/Zr-rich particles confirmed to be Al_3(Sc, Zr) are not distributed congruously in EG and CG regions (Fig. 8a). The

primary Al_3(Sc, Zr) particles with larger sizes are concentrated in the EG region and are mainly distributed near the grain boundaries, while secondary Al_3(Sc, Zr) particles are uniformly distributed in the CG region. The solidification conditions of the melt pool result in the concentration of the primary Al_3(Sc, Zr) particles at the bottom of the pool or remelting zone and lead to the formation of the EG region [22]. In contrast, the Sc/Zr elements in the CG region are supersaturated in the matrix, and then form the secondary Al_3(Sc, Zr) during the direct aging treatment [29]. Thus, inconsistent distributions of primary and secondary Al_3(Sc, Zr) particles are formed.

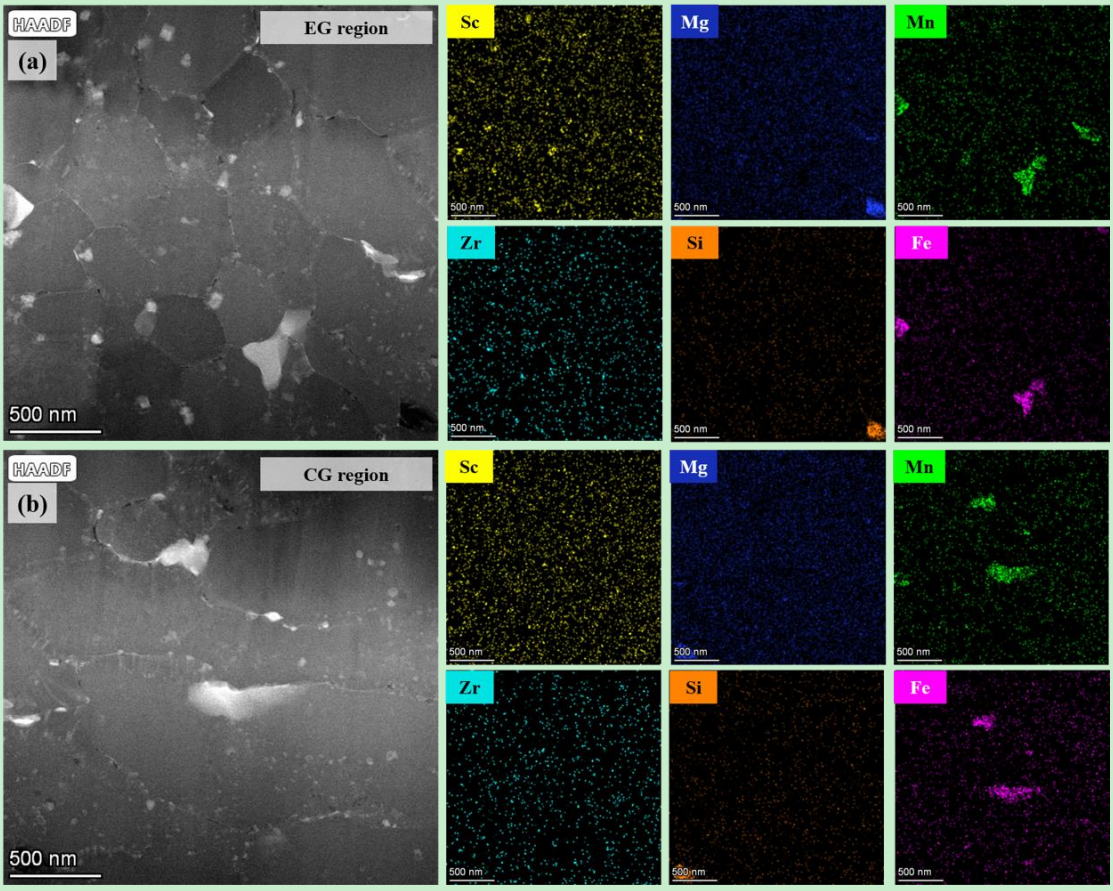

Fig. 8. STEM-EDS mapping (left) HAADF images showing EG (a) and CG (b) regions of Al–Mg–Sc–Zr alloy with numerous second phase; (right) EDS mapping showing elements distribution, in order, is Sc, Zr, Mg, Si, Mn, Fe. These features were pictured

from the TEM foil as shown in Fig 2c.

3.2 Static mechanical properties

3.2.1 Microhardness

According to the Hall–Petch relation, the grain size has a crucial influence on the static mechanical properties of the material, which inevitably results in a nonuniform deformation between the coarse and fine grain regions of the LPBF-fabricated Al–Mg–Sc–Zr alloy, as confirmed in our previous study [17]. Although the heterogeneous deformation will achieve an additional strain hardening under static loading conditions, it seems that it should be avoided under dynamic loading conditions [58,59]. The concentration of deformation in small areas reduces the overall fatigue resistance of the material. After the heat treatment, this mechanical inhomogeneity due to the Hell–Petch relationship may be mitigated by secondary Al_3(Sc, Zr) phases, which are mainly precipitated in the CG region (Fig. 9). To analyze the extent of mechanical heterogeneity for the directly aged LPBF-fabricated Al–Mg–Sc–Zr alloy, a microhardness test was carried out. Fig. 9c and f show the microhardness distributions of the LPBF-fabricated Al–Mg–Sc–Zr alloy for the XY and XZ planes, respectively, which were tested at the locations shown in Fig. 1b. Although the coarse and fine grains have different morphologies and dimensions, they exhibit very similar microhardnesses in both XY and XZ planes. EGs still possess a higher hardness, while the gap between the EG and CG is reduced to within 10 HV, as shown in Fig. 9b and e. The average hardness for the XY plane is similar to that of the XZ plane,

170.0 ± 11.3 and 172.1 ± 5.3 HV, respectively. The subtle difference in hardness is due to the introduction of texture in the CG region [60].

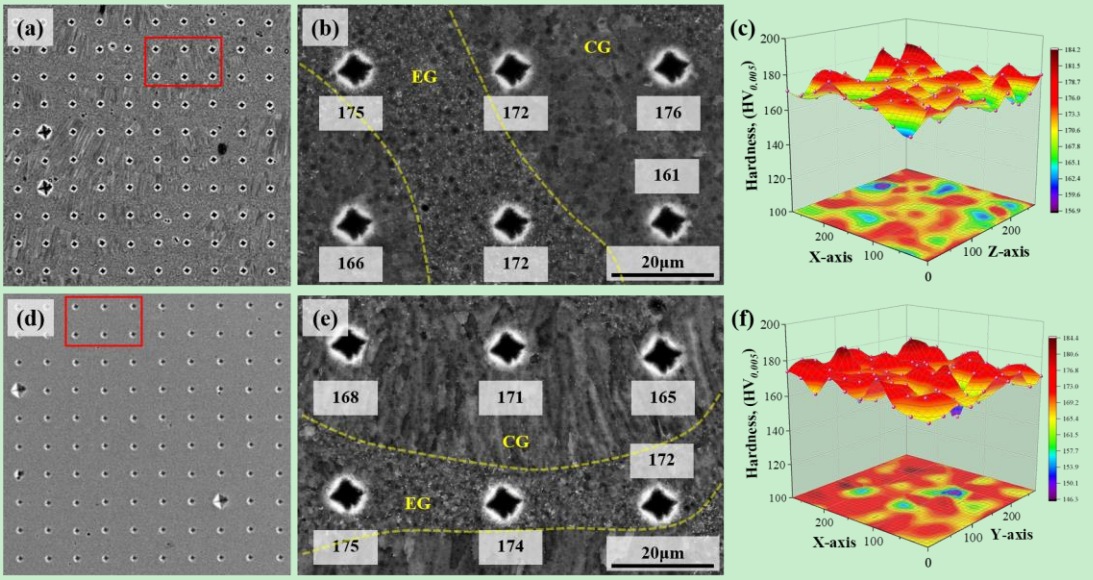

Fig. 9. Overall microhardness images, local enlargement showing the difference of microhardness in the EG and CG regions and microhardness maps of LPBF-fabricated Al–Mg–Sc–Zr alloy in XY plane (a, b and c) and XZ plane (d, e and f).

3.2.2 Tensile properties

The tensile engineering stress–strain curves of the LPBF-fabricated Al–Mg–Sc–Zr alloy in the TD and PD under aging conditions are shown in Fig. 10a. The yield strength (YS), ultimate tensile strength (UTS), elongation to failure (ε_f) and Young's modulus (E) in the TD were determined to be 508.4 MPa, 536.3 MPa, 13.7%, and 72.7 GPa, respectively, while those of the PD sample were 502.4 MPa, 530.2 MPa, 14.4%, and 72.8 GPa, respectively, as listed in Table 4. The deformation energies (UT) of two sample series were also calculated by using the area underneath the tensile curve: UT = $\int_0^{\varepsilon f} \sigma d\varepsilon$. The UT of the TD specimen is 6979 U slightly lower

than that of the PD specimen, 7298 U. The anisotropy is not apparent, which is consistent with the low MUD obtained by the EBSD data (Fig. 6c and d). Similar results were reported by Schmidtke et al. [61]. The good mechanical properties, which are comparable to those of traditional high-strength wrought Al alloys and other LPBF-fabricated Al alloys [6], are attributed to the high grain boundary and precipitation strengthening. Both PD and TD samples exhibit a yield drop and discontinuous yielding behavior during the uniform plastic deformation stage, which is related to a lack of mobile dislocations. It may result from the pinning effect of the Cottrell atmosphere, grain-refinement (especially for EG), and annealing treatment [29]. Then, a slighter strain hardening after yield is obtained according to the stress–strain curves in both deposition directions compared to the as-built state [29], which leads to YS/UTS of 0.965 and 0.972 for TD and PD, respectively, resulting from the less pronounced deformation heterogeneity and thus less dislocation strengthening [62].

The overviews of fracture morphologies of the TD and PD samples are shown in Fig. S3. Both of them have cup-and-cone fracture surfaces. However, their fibrous zones of tensile fractographs are different, presented in Fig. 10b – d. The TD sample (Fig. 10b and c) shows columnar-like morphology covered with cleavage facets and dimples (diameter around 0.62± 0.16 μm), while the PD sample (Fig. 10d and e) shows quasi-cleavage features (tearing ridge) with dimples (diameter around 0.69 ± 0.23 μm). Both of them indicate a mixed mode of ductile and brittle fracture. It is reminiscent of the microstructure distribution in Fig. 6a and b, which suggests that the

crack initiation and propagation are aided by the microstructure.

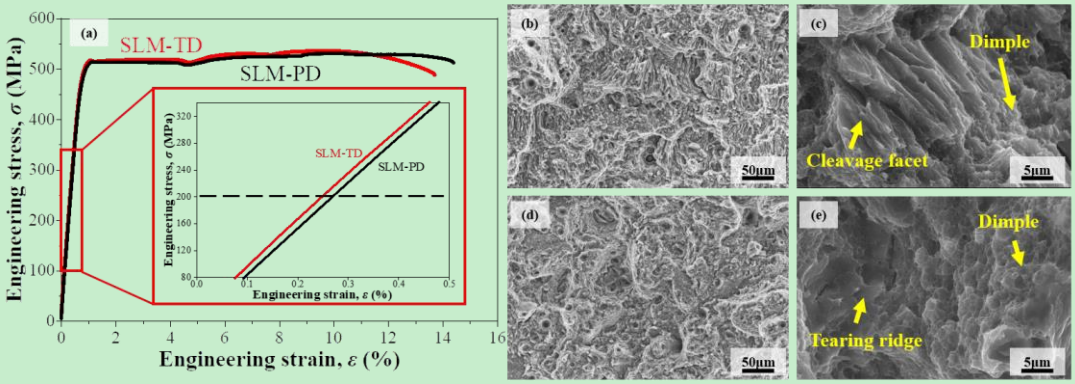

Fig. 10. (a) Representative engineering stress–strain curve of LPBF-fabricated Al–Mg–Sc–Zr alloy in TD and PD. Representative fractographs obtained from (b, c) TD and (d, e) PD specimens.

Table 4 Mechanical properties of LPBF-fabricated Al–Mg–Sc–Zr alloy in TD and PD

Sample	YS (MPa)	UTS (MPa)	ε_f (%)	E (GPa)	*UT (U)*	σ_f (MPa)
TD	509 ± 2	536 ± 1	14.5 ± 0.8	72.1 ± 2.4	6979	100.5
PD	503 ± 2	530 ± 2	14.9 ± 0.5	72.2 ± 1.5	7298	57

3.3 Fatigue properties

The fatigue *S–N* data of the LPBF-fabricated Al–Mg–Sc–Zr alloy in the TD and PD are presented in Fig. 11a. Two curves fitted well with the Basquin equation as shown in Eq. 1:

$$\sigma_a = \sigma_f' \cdot (2N_f)^b \quad (1)$$

Where σ_a and N_f are the stress amplitude and the fatigue life, and σ_f' and b are the

fatigue strength coefficient and the fatigue strength exponent [63]. The fatigue data of the TD series shows a higher scatter than the PD series, which can be attributed to their fewer big defects than those for the PD, as shown in Fig. 3 and 4. Notably, the fatigue strength (σ_f) (calculated by the staircase method [64] and relevant process shown in Fig. S4) of the TD group was 100.5 MPa, considerably higher than σ_f of the PD group (57 MPa). The fatigue strengths were compared to those of Al–Mg–Sc–Zr alloys prepared by other processes, other LPBF-fabricated Al-based alloys, and traditional high-strength Al, as shown in Fig. 11b. To better synthesize the fatigue strengths under varied stress ratios (R), the values are presented with the effective stress amplitude (σ_e) at a stress ratio of –1, which were calculated using the Smith-Wastson-Topper's (SWT) model as shown in Eq. (1) [65]:

$$\sigma_e = \sigma_{max}\sqrt{2/(1-R)} \quad (2)$$

where σ_{max} is the applied maximum stress and R is the applied stress ratio. The TD specimens exhibited a better combination of σ_e and UTS than those of the conventional Al–Mg–Sc–Zr alloys and LPBF-fabricated AlSi10Mg alloy [40,66–68] and similar to that of a wrought 7075-T651 alloy. However, the PD specimens exhibited a relatively low fatigue strength, despite the slightly lower tensile strength than that of the TD specimens. In general, fatigue strength and tensile strength are strongly interdependent in traditional wrought materials[59]. However, their defects and microstructure are more homogeneous and present less detrimental effects compared to the pore, the LoF, and the inhomogeneous microstructure in the LPBF-fabricated Al–Mg–Sc–Zr alloy. Therefore, the exceptionally low fatigue strength

might indicate an underlying mechanism that can accelerate the fatigue failure in the PD group. The anisotropy of the fatigue strength is crucial for the design and manufacturing of engineering parts. Therefore, it is necessary to clarify the mechanism for the anisotropy of the LPBF-fabricated Al–Mg–Sc–Zr alloy.

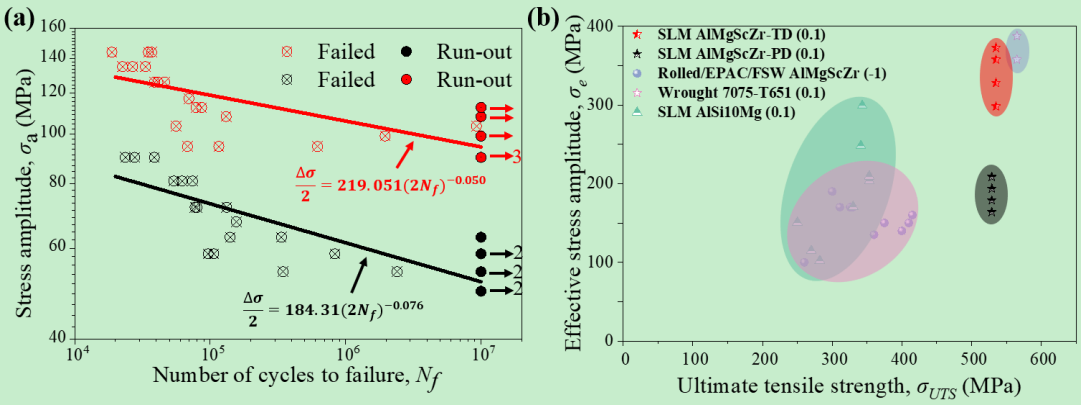

Fig. 11. (a) *S–N* curves of LPBF-fabricated Al–Mg–Sc–Zr alloy in TD and PD. (b) The comparison of fatigue strength and UTS of the LPBF-fabricated Al–Mg–Sc–Zr alloy in TD and PD with those of Al–Mg–Sc–Zr alloy prepared by other process, LPBF-fabricated AlSi10Mg alloy and traditional high-strength Al.

Fig. 12 shows the fracture surfaces in both PD and TD. The whole fatigue fracture surfaces of the TD and PD samples can generally be divided into three regions: crack initiation, crack propagation, and fast fracture regions. The crack is always initiated from the surface and irregular defect, which can be considered a critical defect for crack initiation, as shown in Fig. 12b and d, because of the higher stress concentration of the surface defect than that of the internal defect [69]. The details of these defects shown in Fig. 12b and d (the insets) prove they are LoFs. Notably, the critical defects of the TD and PD specimens with comparable numbers of

cycles share similarities in terms of location, shape, and size, while the difference in σ_a is 36 MPa. According to the flatness of the fracture surface, the crack propagation areas on both PD and TD samples are subdivided into two regions: crack propagation region (I) with a smooth surface and crack propagation region (II) with a surface with scratches and grooves, which can also be observed in Fig. 13. This is correlated to the escalated crack driving force [70]. When the advancing crack has reached a critical size, the specimen raptures rapidly along the maximum shear stress direction and a shear lip with an angle of 45° with respect to the LD is obtained.

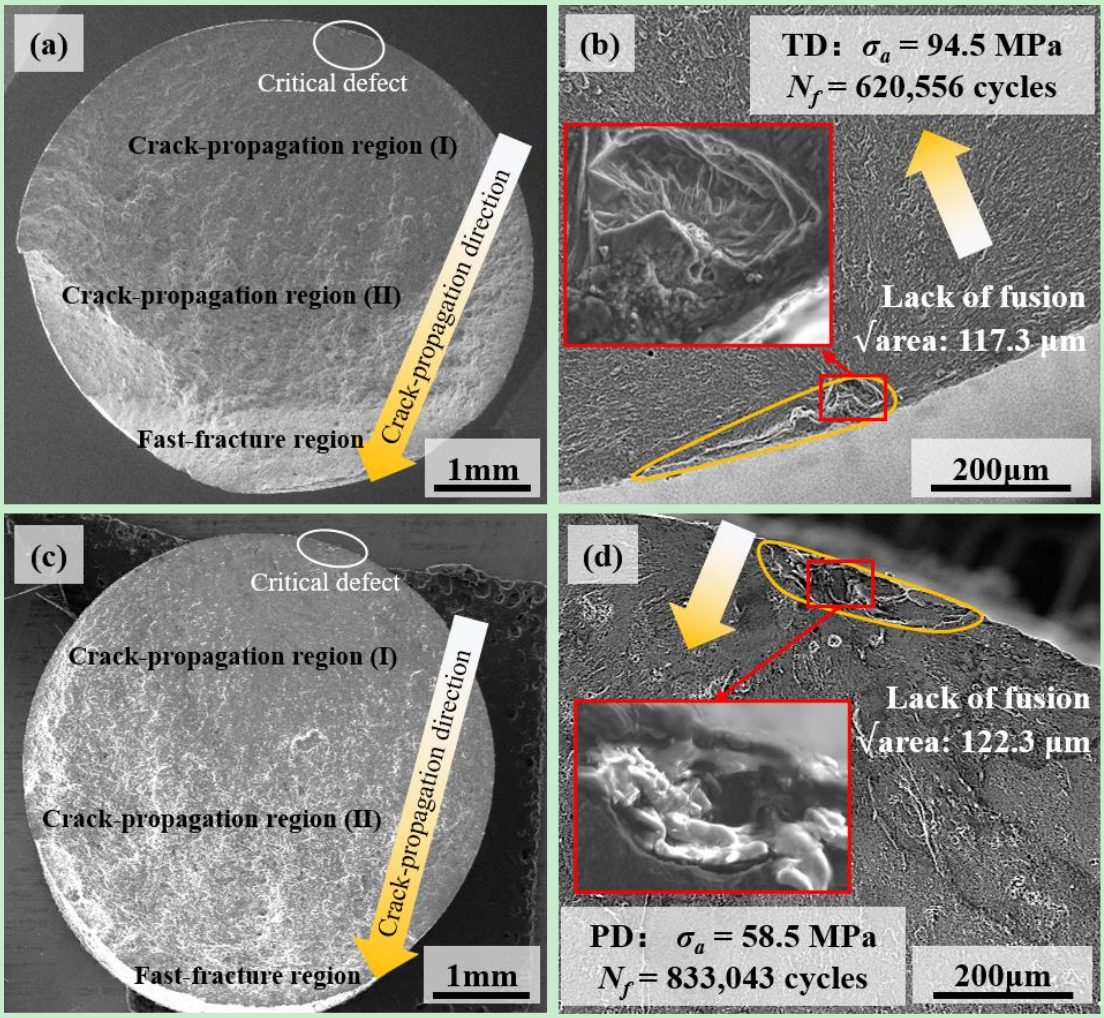

Fig. 12. An overview of fracture morphologies of failed Al–Mg–Sc–Zr specimen and amplification of critical defect which acts as crack origin in TD (a, b) and PD (c, d).

Fig. 13 shows the crack propagation path and detailed EBSD maps. Similar to the above fracture surface, two different crack propagation regions are classified based on the crack curvature on both PD and TD samples: crack propagation region (I) with a straight crack path and crack propagation region (II) with a tortuous path. In addition, the ratios of the EG/CG regions of the TD and PD specimens encountered by fatigue crack are different. For the crack propagation region (I), the simple diagrammatic drawing in Fig. 13a and d (insets) shows that the TD specimen has a higher ratio of EG/CG regions. The shape of the molten pool is obtained from Fig. 5a, which is marked by a red line. For the crack propagation region (II), Fig. 13c and f show that the crack on the TD sample alternately passes CG and EG regions, while the crack on the PD sample mainly passes CG regions. Therefore, the crack on the TD sample encounters more EG regions than that of the PD sample.

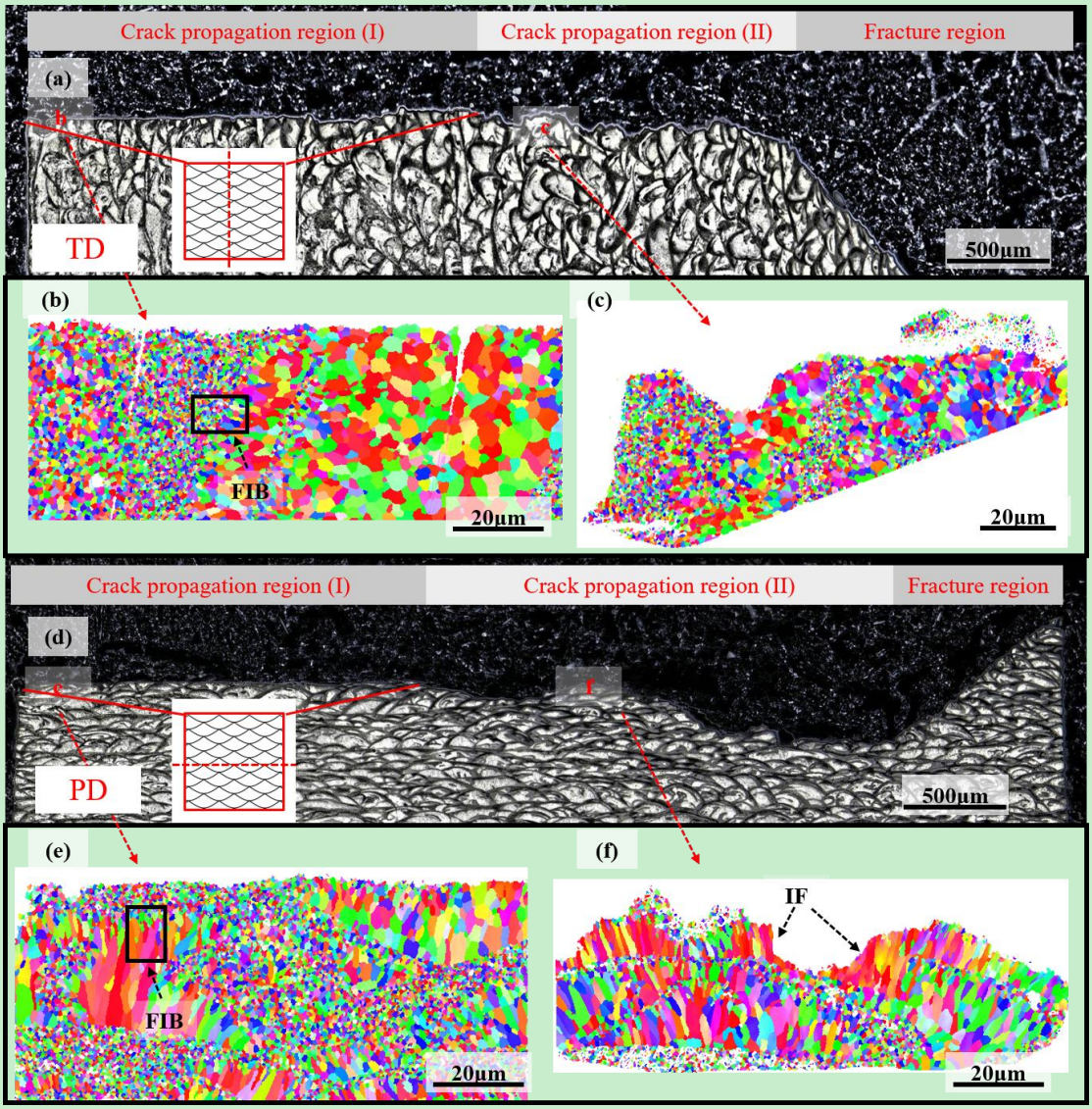

Fig. 13. OM images and EBSD maps of the crack propagation in TD (a, b and c) and PD (d, e and f).

4. Discussion

4.1 Effect of defects on the anisotropic fatigue

The anisotropic fatigue was also observed in other additive manufacturing metallic materials (such as TC4, alloy 718, and steel) [51,60,71,72]. A consistent phenomenon is observed where the defect, particularly the LoF with a flattened shape

and large volume, contributes to the most adverse effect on the fatigue properties. In addition, these LoFs with flattened shapes are always distributed on the laser track between successive layers, leading to different degrees of surrounding stress concentration in different LDs. Afkhami et al. [51] reported that, in vertical samples subjected to an external loading (PD), the sharp corner of the LoF results in a higher stress concentration and lower stress concentration in the horizontal direction (TD). A higher stress concentration implies that the PD samples exhibit a higher true stress around the defect under the same load and are more likely to initiate crack formation. In addition, Xu et al. [60] indicated that a large defect projection area on the plane perpendicular to the building direction enhances the probability of main crack connection and accelerates the crack propagation. Thus, a lower fatigue performance can be expected.

Similar shape, size, and distribution of defects were obtained in this study by the XRT results (Fig. 3 and 4), which demonstrated that these large irregular LoFs have the most detrimental role in the fatigue properties [73,74]. Consequently, it is reasonable to consider that they have a crucial role in the anisotropic fatigue properties. For defect and fatigue properties, the Kitagawa–Takahashi diagram (K–T diagram) [75] is often used to describe their relationship. The main formula is

$$\Delta K_{th} = \Delta\sigma F_w \sqrt{\pi \sqrt{area}} \quad (3)$$

where ΔK_{th} is the long crack growth threshold [42], F_w is a geometric factor depending on the location of defects (0.5 for internal, 0.65 for surface), $\Delta\sigma$ is the stress amplitude applied to the specimens, and $\sqrt{area}$ is the Murakami's parameter

[75] to express the defect size defined as a smooth contour circumscribing the irregular defects shape as shown in Fig. S5 [49]. To evaluate the value of ΔK_{th}, two points were taken as the critical point: one failed sample (99 MPa, 73.7 μm) with the minimum ΔK_{th} as shown in Table 5 and one run-out sample (112.5 MPa, 60 μm) that defected by XRT in our previous work [76], so that ΔK_{th} = 0.876 MPa $m^{1/2}$.

The relationship between the defect size and stress amplitude is shown in Fig. 14. The surface defect depicted by the red solid line has a lower tolerance than that of the internal defect (black dotted line). This can explain the crack initiation always by a surface defect. As the stress amplitude increased, the Murakami's parameter decreased. The experimental stress amplitudes of the two groups were divided by the line of stress amplitude of 90 MPa. This means that the TD specimens will not fail in the presence of the same-sized surface defects as the PD specimens, which fail during fatigue tests. For example, the critical size of surface defects at fatigue strength (100.5 MPa) on the TD sample is 63 μm, whereas that on the PD sample is 181 μm. Thus, to consider the role of defects in the fatigue anisotropy, the critical defect sizes of the crack initiation (the Marukami's parameter) observed using SEM are presented in Fig. 14. The circles represent the TD group specimens, while the triangles represent the PD group specimens. The TD group is located at the top right of the red solid line, which implies that the defects at crack initiation in these specimens do not support the specimen to undergo 10^7 cycles at the stress amplitude. When the point is more to the right side, the cycle life is shorter. However, for the PD group, although similar defect sizes at crack initiation were observed, they still cause fatigue fracture with similar

lifetimes at a lower σ_a. In particular, the points depicted by the red circle of the PD samples in the safe regime are still ruptured. As the defects on this red line were determined by ΔK_{th} calculated for the TD group, points located in the safe regime imply that ΔK_{th} for the PD group was smaller and that it had a lower resistance to crack initiation and propagation. Therefore, it is reasonable to speculate that other factors affect the anisotropy of the fatigue performance.

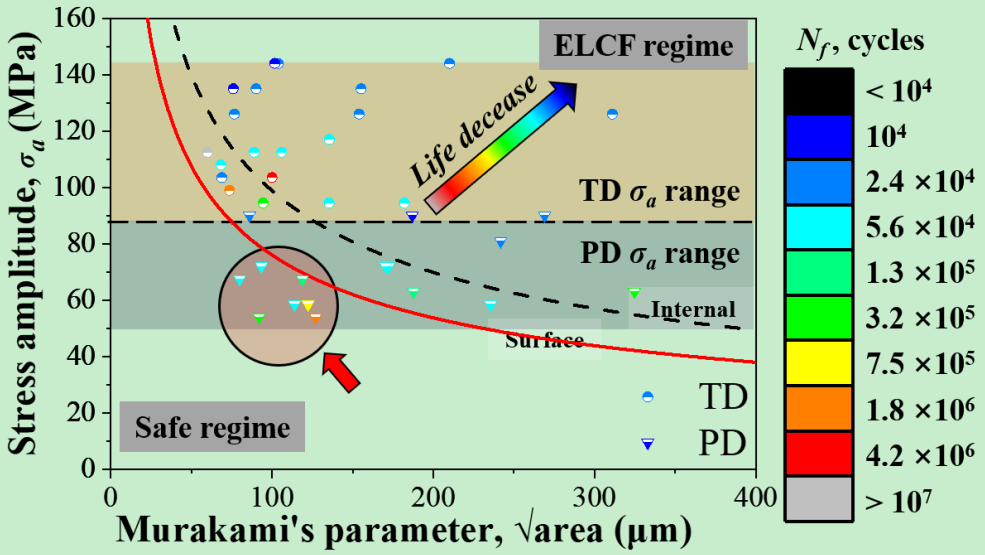

Fig. 14. Calculated stress amplitude (σ_a) as a function of Murakami's parameter for LPBF-fabricated Al–Mg–Sc–Zr alloy. The ELCF region is Extreme Low cycle fatigue.

Table 5 Information about fatigue tests and characteristics of defects

	Point number	σ_a (MPa)	N_f (cycles)	$\sqrt{area}$ (μm)		Point number	σ_a (MPa)	N_f (cycles)	$\sqrt{area}$ (μm)
TD group	1*	67.5	$> 10^7$	-	PD group	1	135	18363	366.1
	2	108	$> 10^7$	-		2	90	27676	269.0
	3	144	34974	210.1		3	90	38712	86.1
	4	117	69697	135.5		4	54	$> 10^7$	-
	5	112.5	$> 10^7$	-		5	72	77389	172.2
	6	112.5	78756	106.0		6	58.5	$> 10^7$	-
	7	112.5	86487	89.7		7	67.5	111478	80.3
	8	108	131407	68.3		8	63	336305	324.8
	9	103.5	9270465	100.2		9	63	$> 10^7$	-
	10	99	$> 10^7$	-		10	67.5	156042	118.8
	11	103.5	55920	68.9		11	63	140245	187.8
	12	99	1957299	73.7		12	58.5	96771	235.6
	13	94.5	68044	135.4		13	54	2396482	127.0
	14	90	$> 10^7$	-		14	49.5	$> 10^7$	-
	15	94.5	115937	182.1		15	58.5	833043	122.3
	16	90	$> 10^7$	-		16	54	$> 10^7$	-
	17	94.5	620556	117.3		17	58.5	$> 10^7$	-
	18	90	$> 10^7$	-		18	58.5	106407	114.2
	19	144	36975	104.2		19	54	345590	92.3

20	144	18823	101.7	20	49.5	$> 10^7$	-
21	135	26777	155.2	21	72	80006	170.6
22	135	22511	76.1	22	72	132309	93.4
23	135	33275	90.1	23**	90	23605	-
24	126	46074	154.3	24	81	53847	241.8
25**	126	41095	-	25**	81	74172	-
26	126	38797	76.7	26**	81	62048	-

* It was not included in the staircase calculation.

** The fracture surface was damaged.

4.2 Effect of the microstructure on the anisotropic fatigue properties

4.2.1 Heterogeneous structure

The Al_3(Sc, Zr) phases exhibit an inhomogeneous distribution, with primary Al_3(Sc, Zr) precipitating in the EG region, while the secondary Al_3(Sc, Zr) precipitates in the CG region. This inhomogeneous precipitation behavior weakens the hardness gap resulting from the Hall–Petch relationship between the CG and EG regions (Fig. 9). The Al_3(Sc, Zr) phases have an $L1_2$ ordered structure and are coherent with the α-matrix; the main difference is the size. According to the TEM results (Fig. 7 and 8), the size of the primary Al_3(Sc, Zr) phase is tens of nanometers, while the size of the secondary Al_3(Sc, Zr) phase is smaller than 5 nm. According to the classic precipitation theory, an increase in particle size results in a transition from particle shearing (also referred to as antiphase boundary (APB) mechanism) to Orowan dislocation looping. Watanabe et al. [77] reported that the critical size of the

mechanism shift for the Al_3(Sc, Zr) phase is approximately 4.8 nm. Therefore, it is reasonable to speculate that the resistance of the primary Al_3(Sc, Zr) to dislocation is the Orowan mechanism and APB mechanism for the secondary Al_3(Sc, Zr). This leads to the different resistances of the two types of particles to cyclic loading. For the APB mechanism, planar slip, a feature of the APB mechanism, results in dislocations continuously passing particles along a single plane and simultaneously disrupting the short-range order (SRO) structure of Al_3(Sc, Zr) particles [78]. Thus, cyclic softening occurred. This has been demonstrated in Al–Mg–Sc alloys with Al_3Sc (4 nm) [79]. For the Orowan mechanism, the dislocation loop in the second phase with the SRO structure is unbroken. Thus, no cyclic softening occurred [77]. This difference leads to the EG region possessing a better resistance to cyclic loading than the CG region in the aged LPBF-fabricated Al–Mg–Sc–Zr alloy.

In addition, the microtextures of the two grain regions are important to the crack propagation process because the twist and tilt angles of the crack-plane deflection at grain boundaries are the main factors affecting the fatigue crack growth [80]. The crack path tilting reduces the effective driving force, while the twisting controls the fractured area for cracks to pass through the grain boundaries [80,81]. The EBSD results (Fig. 6) show that the CG region has a preferred orientation, while the EG region does not have preferred orientation. This implies that the EG region possesses larger tilt and twist angles than those of the CG region. Therefore, the resistance to crack propagation in the EG region is higher than that in the CG region.

Fig. 15 depicts the difference of the fatigue striations between EG and CG regions

at the same location of TD and PD specimens. The fatigue striations are the traces left by the fatigue crack propagation and can be used to reflect the fatigue crack propagation [80,82]. The fatigue striations in the EG region are shallower with shorter distance than in the CG region both in the PD and TD specimens, indicating that the CG has lower fatigue resistance, which is consistent with above discussion.

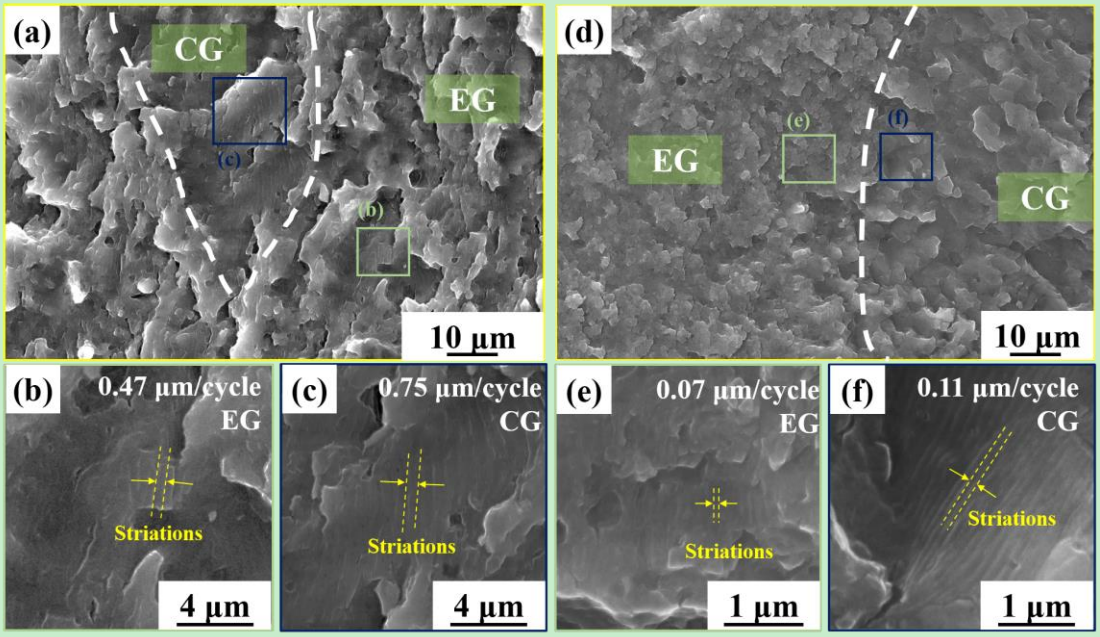

Fig. 15 Fatigue striations in TD (a, b and c) and PD (d, e and f). (b) and (e) showing the fatigue striations in the EGs. (c) and (f) showing the fatigue striations in the CGs.

The EG region has better fatigue properties than the CG region because it has a slight cyclic softening effect and strong crack deflection effect. Moreover, the percentage of EGs encountered by the crack is larger on the TD sample than on the PD sample, as shown in Fig. 13. Therefore, the TD group had a better fatigue performance than that of the PD group.

4.2.2 CG orientation

According to the above EBSD analysis, the average grain size of the EG region

is 0.6 ± 0.2 μm, while that of the CG region is 1.8 ± 0.5 μm. Most grains in the EG region are UFGs (0.1–1 μm) without formation of dislocation configuration, which can store the strain in the case of static tension [62,83,84]. To clarify the mechanism of fatigue, the dislocation configurations were determined in the EG and CG regions on the TD and PD samples, as shown in Fig. 15. The EG regions on the TD and PD samples lack dislocations, as shown in Fig. 15a and c. The dislocation configuration and intergranular cracking in the CG region are not the same for the TD and PD FIB foils, which were obtained from the near fatigue fracture surface, as shown in Fig. 15a–d. Dislocations and few intergranular cracks are visible in the TD section, whereas an inverse phenomenon appears in the PD section.

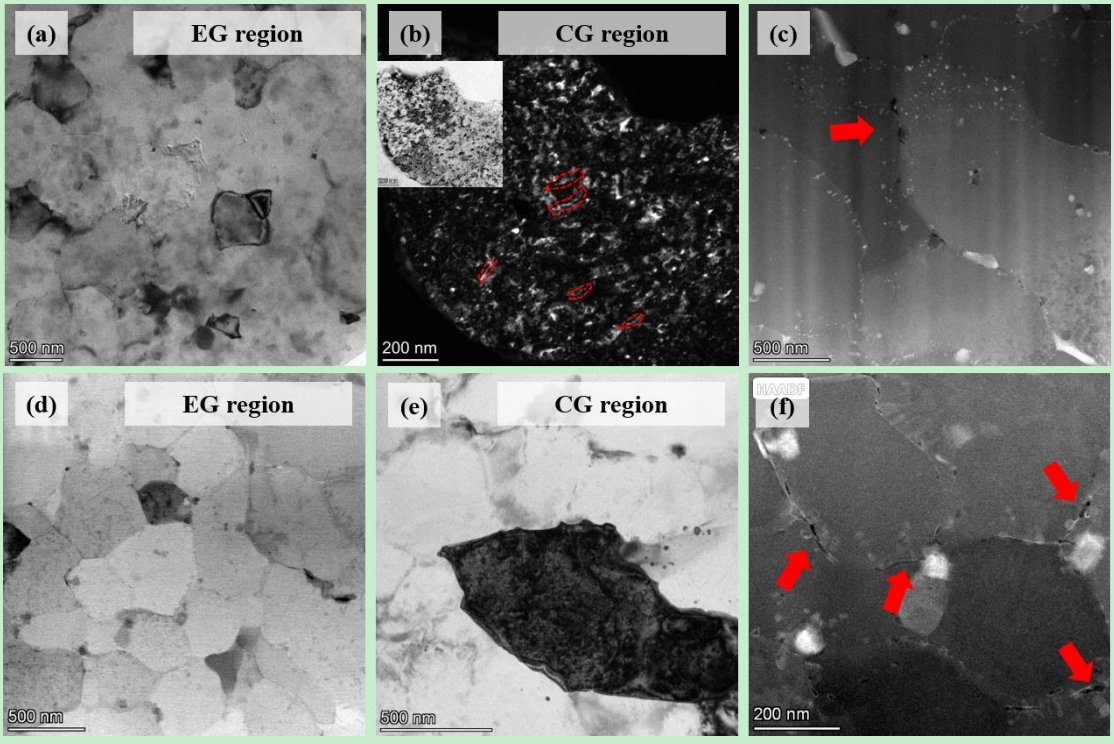

Fig. 16. Dislocation configuration in EG and CG regions in TD (a, b) and PD (d, e). The inset in b is its bright field image. The intergranular cracking in TD (c) and PD (f). The red dotted line representing dislocation and the red arrows representing the

intergranular cracking.

As mentioned above, the presence of numerous secondary $Al_3(Sc, Zr)$ phases forces the dislocation motion by the APB mechanism so that the planar slip mode is suggested for dislocation glide [78]. Furthermore, the deformation leads to nucleation and multiplication of dislocation within grains. With a sufficient deformation, the dislocation rearranges in a subgrain boundary and saturates to a certain value. The microstructural characteristic of saturated subgrains is such that the interior of the subgrain is almost free from dislocation and dislocation concentrates in 2D subgrain boundaries at steady-state deformation [83,85]. The dislocation configuration is well correlated with the distance between dislocation sources and sinks, which is equal to the size of the subgrain (w), which can be calculated by [83]

$$w = k_w b \frac{G}{\sigma_t}, \quad (4)$$

where k_w is a numerical factor, 28 for the Al–Mg alloy [86,87], b is the magnitude of the Burgers vector (0.286 nm for Al), G is the shear modulus (26.2 GPa for Al), and σ_t is the true stress. Considering the plastic zone at the crack tip of the aluminum alloy, the stress concentration was limited to the yield strength. The steady-state deformation of grains under fatigue conditions was between the yield and fatigue. Thus, by substituting σ_t with the average value of the yield strength and fatigue strength (304.8 MPa for TD and 280 MPa for PD) into Eq. 3, the sizes of the subgrains were determined to be 0.71 μm for the TD sample and 0.77 μm for the PD sample.

However, it is not sufficient to explain the different dislocation patterns in the CG regions of the TD and PD samples (Fig. 15c and e) through the relationship between *w* and grain size, which can be attributed to the grain size in the CG region. The sizes of the subgrains of the TD and PD specimens are similar. However, the angle between the slip plane and long axis of the CG affects the distance between the dislocation source and sink. The size of the subgrains of the TD and PD samples conforms to the short axis of the CG and is smaller than the long axis of the CG. Thus, it is reasonable to speculate that, if the dislocation moves along the short axis of the CG, it will be absorbed by the grain boundary, while the dislocation moving along the long axis will be hardly absorbed by the grain boundary.

To discuss this mechanism, it is necessary to understand the relationship between the slip plane and grain orientation. Fig. 16 shows the grains with < 100 >, < 110 >, and < 111 > crystal orientations along the building direction (angle < 20°) according to the EBSD data (Fig. 6b). The grain orientation is random in the EG, while the grains have grown preferentially in the CG. The major crystal direction of CGs was < 100 > || BD, followed by the grains with the < 110 > || BD orientation.

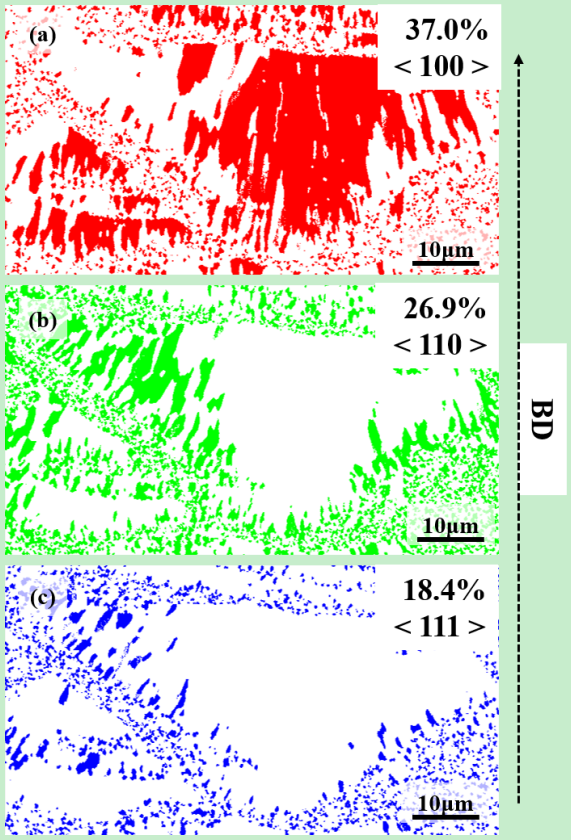

Fig. 17. The grains with < 100 >, < 110 >, and < 111 > crystal orientations along the building direction (angle < 20°).

The EBSD maps derived from IPF || BD at the crack propagation region (I) in the same location of the FIB foil are presented in Fig. 17. Because of the limitation of EBSD image pixel and resolution, the crystal profiles of the FIB foil cannot perfectly correspond to the FIB foil, but the CG crystal orientation can be appropriately obtained by the EBSD maps. Two representative grains with < 100 > || BD and < 110 > || BD orientations were selected from Fig. 17b and d, respectively, for discussion. Under the uniaxial load, the dislocations slip along the slip system that exceeds the resolved shearing stress. According to the Schmid's law, the resolved shear stress (τ) can be calculated by

$$\tau = \sigma \cos(\alpha) \cos(\beta), \quad (5)$$

where σ is the external stress, α is the angle between the normal direction of the slip plane and direction of the external stress, β is the angle between the direction of the slip direction and direction of the external stress, and $\cos(\alpha)\cos(\beta)$ is the Schmid factor (m_s). Considering the 12-slip system in an FCC crystal, 12 different Schmid factors were obtained.

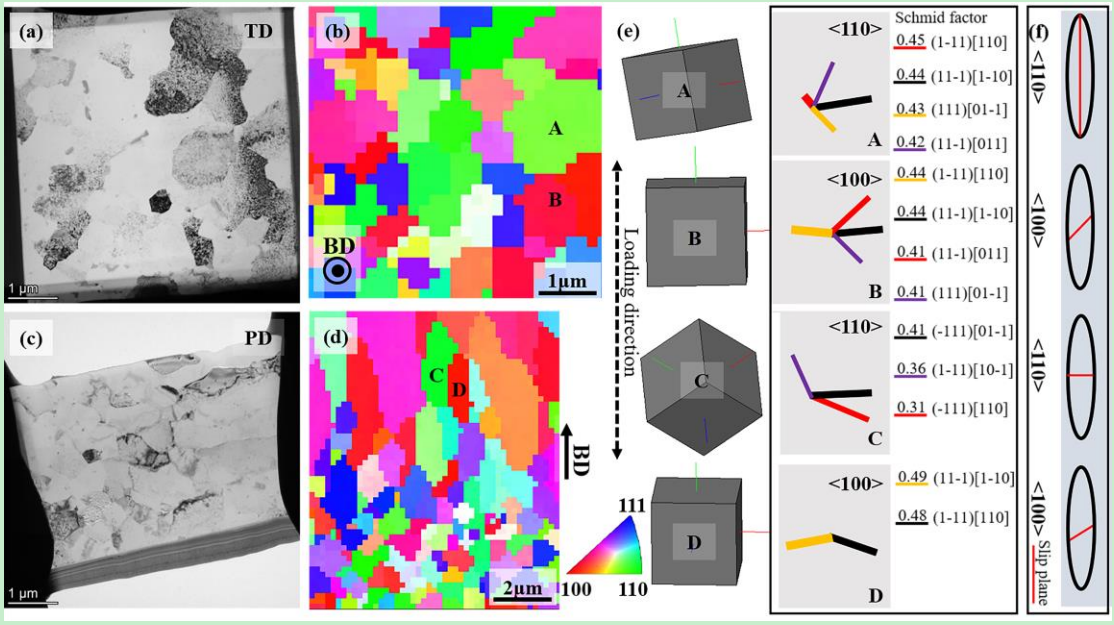

Fig. 18. The overview of FIB-foil image and corresponding EBSD maps, which is enlargement of the red solid line box in Fig. 15, in TD (a, b) and PD (c, d), both of the EBSD maps derived from direction IPF || BD. (e) Slip trace maps and corresponding Schmid factor values for each slip system in grains. (f) Schematic of slip plane of grains with different orientations.

The crystal orientation, Schmid's factors, and corresponding slip systems are shown in Fig. 17e. For the PD specimen, the directions of the slip system of the < 100 > || BD and < 110 > || BD grains with high m_s values are inclined at 45° and

parallel to the short axis of the grain, as illustrated in Fig. 17f. For the TD specimen, the < 100 > || BD grain has a slip direction with a high m_s inclined at 45° with respect to the short axis, while for the < 110 > || BD grain, its crystal growth direction can be used as an effective slip system for dislocation motion. For example, for grain A, m_s of the [110] grain growth direction is 0.45, which is the highest in its 12-slip system. Therefore, after emission from the source, the dislocation slipped along the long axis of the CG, encountering the boundary of the subgrain.

This potential mechanism was also demonstrated in the crack propagation region (I). Fig. 18 shows the fractographs of the TD and PD samples with clear fatigue striations, which are parallel to each other and perpendicular to the local crack propagation direction. In the CG region of the PD specimen (Fig. 18d), the main crack truncates the CG and shows a circular surface. In addition, the fatigue striations are distributed parallel to the surface, as indicated by the red dashed lines. The intergranular cracks at the grain boundaries parallel to the fatigue striations are visible (also observed in Fig. 15f), which represents the formation of dislocations emanated from one side of the grain boundary and subsequently absorbed by the other side of one grain. Cracking becomes an important manner to accommodate the deformation of grains that cannot accommodate dislocations [80]. For the TD specimen, the crack propagation direction defined by the fatigue striations is parallel to the long axis of the CG. Unlike the single plane for crack propagation of the CG on the PD sample, a dual-plane is formed with the formation of a secondary crack in the vicinity, which implies a complex stress state in the CGs of the TD sample.

Therefore, dislocations are absent in the CGs of the PD sample. This results in irreversible deformation, cyclic softening [62,67,84,86,88], and absence of formation of multiple slip planes, which can disperse the crack driving force. Therefore, the PD group exhibited a lower crack propagation resistance than that of the TD group.

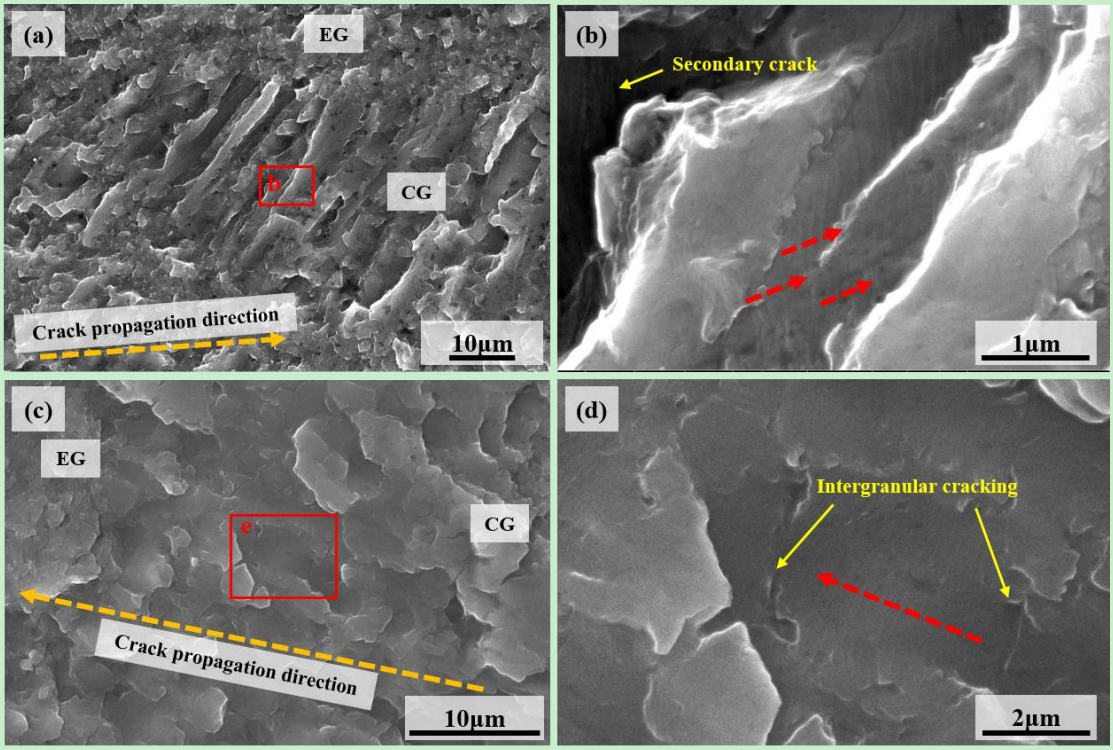

Fig. 19. Fractographs of samples in TD (a, b) and PD (c, d). (b) and (d) representing the detail of fatigue striations in CG region. The red arrows representing fatigue striation forward direction.

The effect of defects and microstructure on the anisotropic fatigue mechanisms is illustrated in Fig. 19. In general, the total fatigue life (N_f) is the sum of cycles for crack nucleation and initiation (N_i) and propagation (N_p). As for N_i, the fatigue crack initiation is mainly affected by the defects. In this study, the distribution of the defect that orient within the build plane causes higher stress concentrations under loading

conditions in the PD specimens than in the TD specimens, which results in lower critical loads for crack initiation. Thus, the lower N_i of the PD group than that of the TD group can be expected. This may be the main reason for anisotropic fatigue property due to N_i account for most fatigue life. As for N_p, we focused on the influence of microstructure on fatigue crack propagation, which also contributes to anisotropy. Regarding crack propagation region (I), the strain concentration in the movable slip system near the crack tip dominates the crack propagation. As shown in Fig. 19 (b), the CG region possesses a lower fatigue resistance than that of the EG region at the crack propagation region (I), owing to the stronger cycling softening and weaker crack deflection effect. In addition, Fig. 19 (c) shows that the fatigue crack passes through more equiaxed regions in the TD sample than in the PD sample. Thus, from the aspect of heterogonous grain distribution, the TD sample exhibits a high fatigue crack propagation resistance. On the other hand, as shown in Fig. 19 (d), the CG with the <110> || BD orientations in the TD specimens, which can stock the dislocations with a high fatigue resistance and compatible deformation capability. Thus, these CGs can also help to impede the crack propagation. Moreover, at the crack propagation region (II), the crack can propagate without passing through the EG region in the PD sample, which is different from the behavior in the TD sample (Fig. 19 (e)). Therefore, the crack initiation and propagation in the TD sample are more difficult than those in the PD sample owing to the anisotropic fatigue properties.

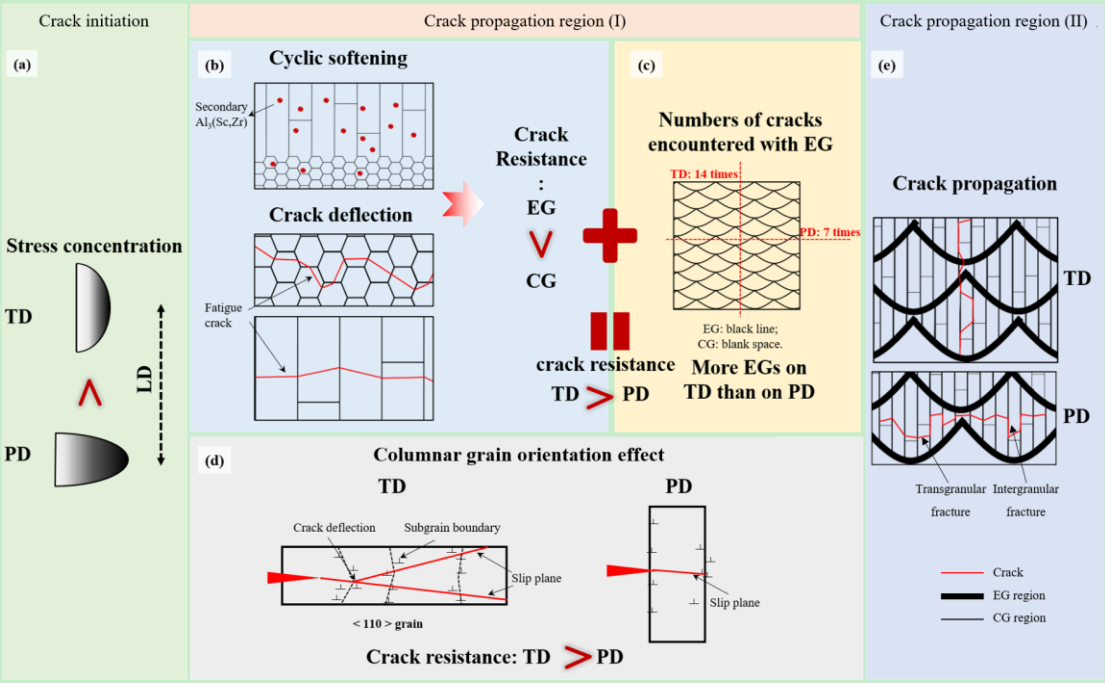

Fig. 20. Schematic of effects of defect and microstructure on anisotropic fatigue. (a) Schematic of stress concentrations of defects. (b) Schematic of softening mechanisms of CG. (c) Schematic of frequency of fatigue crack encounter EG in TD and PD. The shape of molten pool got from Fig. 5a which was depicted by red line. (d) Schematic of effect of columnar grain orientation on crack resistance. (d) Schematic of crack path in the crack propagation region (II).

5. Conclusions

This study was focused on the anisotropic high-cycle fatigue mechanism responsible for crack initiation and propagation in LPBF-fabricated Al–Mg–Sc–Zr alloys. The fatigue properties of the aged LPBF-fabricated Al–Mg–Sc–Zr showed a surprising anisotropy. The fatigue strength of the TD sample was 100.5 MPa, while that of the PD sample was 57 MPa. The following mechanisms were proposed.

(i) With respect to defects, based on the features of defects analyzed X-ray

tomography, the LoF defects in the LPBF-fabricated Al-Mg-Sc-Zr are more important to the fatigue performance than the pores. The LoF defects have irregular shape with longest axis distributing predominantly vertical to the building direction. This feature of LoF resulted in a higher stress concentration in the PD sample than that of the TD sample in the crack initiation stage.

(ii) With respect to the heterogeneous structure, owing to the significant cyclic softening and indistinctive crack deflection of the CG region, it became soft with the decrease in fatigue resistance. Furthermore, the different crack propagation directions led to different CG/EG area ratios for the anisotropic fatigue properties.

(iii) With respect to the CG orientation, in the TD samples, the presence of the CGs with the < 110 > || BD orientation led to a higher fatigue resistance of the TD sample than in the PD sample, owing to the exceptional dislocation formation.

CRediT authorship contribution statement

Zehao Qin: Investigation, Writing-Original draft preparation. **Nan Kang:** Project administration, Writing - review & editing, Methodology, Supervision. **Mohamed El Mansori:** Writing - review & editing. **Zihong Wang:** Methodology, Data Curation. **Haoxiang Wang:** Data Curation. **Xin Lin:** Conceptualization, Funding acquisition. **Jing Chen:** Funding acquisition. **Weidong Huang:** Supervision.

Acknowledgements

This work was supported by National Key Research and Development Plan of China (2016YFB1100102) and National Natural Science Foundation of China (52005411) and the Research Fund of the State Key Laboratory of Solidification Processing (NPU) (2020-tz-02). The authors also appreciate the help from Dr. Ying Ding at Analytical & Testing Center of NPU for FIB milling.

Reference

[1] G. Liu, X. Zhang, X. Chen, Y. He, L. Cheng, M. Huo, J. Yin, F. Hao, S. Chen, P. Wang, S. Yi, L. Wan, Z. Mao, Z. Chen, X. Wang, Z. Cao, J. Lu, Additive manufacturing of structural materials, Mater. Sci. Eng. R. (2020) 100596. https://doi.org/10.1016/j.mser.2020.100596.

[2] M. Schmidt, M. Merklein, D. Bourell, D. Dimitrov, T. Hausotte, K. Wegener, L. Overmeyer, F. Vollertsen, G.N. Levy, Laser based additive manufacturing in industry and academia, CIRP Ann. 66 (2017) 561–583. https://doi.org/10.1016/j.cirp.2017.05.011.

[3] D. Herzog, V. Seyda, E. Wycisk, C. Emmelmann, Additive manufacturing of metals, Acta Mater. 117 (2016) 371–392. https://doi.org/10.1016/j.actamat.2016.07.019.

[4] W.E. Frazier, Metal additive manufacturing: A review, J. Mater. Eng. Perform. 23 (2014) 1917–1928. https://doi.org/10.1007/s11665-014-0958-z.

[5] E.O. Olakanmi, R.F. Cochrane, K.W. Dalgarno, A review on selective laser sintering/melting (SLS/SLM) of aluminium alloy powders: Processing,

microstructure, and properties, Prog. Mater. Sci. 74 (2015) 401–477. https://doi.org/10.1016/j.pmatsci.2015.03.002.

[6] J.J. Lewandowski, M. Seifi, Metal Additive Manufacturing: A Review of Mechanical Properties, Annu. Rev. Mater. Res. 46 (2016) 151–186. https://doi.org/10.1146/annurev-matsci-070115-032024.

[7] Q. Tan, J. Zhang, Q. Sun, Z. Fan, G. Li, Y. Yin, Y. Liu, M.X. Zhang, Inoculation treatment of an additively manufactured 2024 aluminium alloy with titanium nanoparticles, Acta Mater. 196 (2020) 1–16. https://doi.org/10.1016/j.actamat.2020.06.026.

[8] A. Xue, X. Lin, L. Wang, X. Lu, H. Ding, W. Huang, Heat-affected coarsening of β grain in titanium alloy during laser directed energy deposition, Scr. Mater. 205 (2021) 114180. https://doi.org/10.1016/j.scriptamat.2021.114180.

[9] J. Bi, Z. Lei, Y. Chen, X. Chen, Z. Tian, J. Liang, X. Zhang, X. Qin, Microstructure and mechanical properties of a novel Sc and Zr modified 7075 aluminum alloy prepared by selective laser melting, Mater. Sci. Eng. A. 768 (2019) 138478. https://doi.org/10.1016/j.msea.2019.138478.

[10] A. Mehta, L. Zhou, T. Huynh, S. Park, H. Hyer, S. Song, Y. Bai, D.D. Imholte, N.E. Woolstenhulme, D.M. Wachs, Y. Sohn, Additive manufacturing and mechanical properties of the dense and crack free Zr-modified aluminum alloy 6061 fabricated by the laser-powder bed fusion, Addit. Manuf. 41 (2021) 101966. https://doi.org/10.1016/j.addma.2021.101966.

[11] H. Zhang, H. Zhu, X. Nie, J. Yin, Z. Hu, X. Zeng, Effect of Zirconium addition on crack, microstructure and mechanical behavior of selective laser melted Al-Cu-Mg alloy, Scr. Mater. 134 (2017) 6–10. https://doi.org/10.1016/j.scriptamat.2017.02.036.

[12] R. Xu, R. Li, T. Yuan, P. Niu, M. Wang, Z. Lin, Microstructure, metallurgical defects and hardness of Al–Cu–Mg–Li–Zr alloy additively manufactured by selective laser melting, J. Alloys Compd. 835 (2020) 155372. https://doi.org/10.1016/j.jallcom.2020.155372.

[13] K. V. Yang, P. Rometsch, T. Jarvis, J. Rao, S. Cao, C. Davies, X. Wu, Porosity

formation mechanisms and fatigue response in Al-Si-Mg alloys made by selective laser melting, Mater. Sci. Eng. A. 712 (2018) 166–174. https://doi.org/10.1016/j.msea.2017.11.078.

[14] M. Bonneric, C. Brugger, N. Saintier, Effect of hot isostatic pressing on the critical defect size distribution in AlSi7Mg0.6 alloy obtained by selective laser melting, Int. J. Fatigue. 140 (2020) 105797. https://doi.org/10.1016/j.ijfatigue.2020.105797.

[15] J.H. Martin, B.D. Yahata, J.M. Hundley, J.A. Mayer, T.A. Schaedler, T.M. Pollock, 3D printing of high-strength aluminium alloys, Nature. 549 (2017) 365–369. https://doi.org/10.1038/nature23894.

[16] S. Beretta, S. Romano, A comparison of fatigue strength sensitivity to defects for materials manufactured by AM or traditional processes, Int. J. Fatigue. 94 (2017) 178–191. https://doi.org/10.1016/j.ijfatigue.2016.06.020.

[17] Z. Wang, X. Lin, N. Kang, Y. Hu, J. Chen, W. Huang, Strength-ductility synergy of selective laser melted Al-Mg-Sc-Zr alloy with a heterogeneous grain structure, Addit. Manuf. 34 (2020) 101260. https://doi.org/10.1016/j.addma.2020.101260.

[18] R. Li, M. Wang, Z. Li, P. Cao, T. Yuan, H. Zhu, Developing a high-strength Al-Mg-Si-Sc-Zr alloy for selective laser melting: Crack-inhibiting and multiple strengthening mechanisms, Acta Mater. 193 (2020) 83–98. https://doi.org/10.1016/j.actamat.2020.03.060.

[19] Y. Qi, H. Zhang, X. Nie, Z. Hu, H. Zhu, X. Zeng, A high strength Al–Li alloy produced by laser powder bed fusion: Densification, microstructure, and mechanical properties, Addit. Manuf. 35 (2020) 101346. https://doi.org/10.1016/j.addma.2020.101346.

[20] D. Bayoumy, D. Schliephake, S. Dietrich, X.H. Wu, Y.M. Zhu, A.J. Huang, Intensive processing optimization for achieving strong and ductile Al-Mn-Mg-Sc-Zr alloy produced by selective laser melting, Mater. Des. 198 (2021) 15–17. https://doi.org/10.1016/j.matdes.2020.109317.

[21] Q. Jia, P. Rometsch, P. Kürnsteiner, Q. Chao, A. Huang, M. Weyland, L.

Bourgeois, X. Wu, Selective laser melting of a high strength Al[sbnd]Mn[sbnd]Sc alloy: Alloy design and strengthening mechanisms, Acta Mater. 171 (2019) 108–118. https://doi.org/10.1016/j.actamat.2019.04.014.

[22] J.R. Croteau, S. Griffiths, M.D. Rossell, C. Leinenbach, C. Kenel, V. Jansen, D.N. Seidman, D.C. Dunand, N.Q. Vo, Microstructure and mechanical properties of Al-Mg-Zr alloys processed by selective laser melting, Acta Mater. 153 (2018) 35–44. https://doi.org/10.1016/j.actamat.2018.04.053.

[23] X. Wu, Y. Zhu, Heterogeneous materials: a new class of materials with unprecedented mechanical properties, Mater. Res. Lett. 5 (2017) 527–532. https://doi.org/10.1080/21663831.2017.1343208.

[24] Y. Kok, X.P. Tan, P. Wang, M.L.S. Nai, N.H. Loh, E. Liu, S.B. Tor, Anisotropy and heterogeneity of microstructure and mechanical properties in metal additive manufacturing: A critical review, Mater. Des. 139 (2018) 565–586. https://doi.org/10.1016/j.matdes.2017.11.021.

[25] G.J. Fan, H. Choo, P.K. Liaw, E.J. Lavernia, Plastic deformation and fracture of ultrafine-grained Al-Mg alloys with a bimodal grain size distribution, Acta Mater. 54 (2006) 1759–1766. https://doi.org/10.1016/j.actamat.2005.11.044.

[26] Y. Zhu, X. Wu, Perspective on hetero-deformation induced (HDI) hardening and back stress, Mater. Res. Lett. 7 (2019) 393–398. https://doi.org/10.1080/21663831.2019.1616331.

[27] C. Deng, R. Li, T. Yuan, P. Niu, Y. Wang, Microstructure and mechanical properties of a combination interface between direct energy deposition and selective laser melted al-mg-sc-zr alloy, Metals (Basel). 11 (2021). https://doi.org/10.3390/met11050801.

[28] T. Zhao, Y. Wang, T. Xu, M. Bakir, W. Cai, M. Wang, M. Dahmen, Q. Zheng, X. Wei, C. Hong, C. Zhong, P. Albus, T. Schopphoven, A. Gasser, C.L. Häfner, Some factors affecting porosity in directed energy deposition of AlMgScZr-alloys, Opt. Laser Technol. 143 (2021). https://doi.org/10.1016/j.optlastec.2021.107337.

[29] Z. Wang, X. Lin, N. Kang, J. Chen, H. Tan, Z. Feng, Z. Qin, H. Yang, W.

Huang, Laser powder bed fusion of high-strength Sc/Zr-modified Al–Mg alloy: phase selection, microstructural/mechanical heterogeneity, and tensile deformation behavior, J. Mater. Sci. Technol. 95 (2021) 40–56. https://doi.org/10.1016/j.jmst.2021.03.069.

[30] L. Zhou, H. Pan, H. Hyer, S. Park, Y. Bai, B. McWilliams, K. Cho, Y. Sohn, Microstructure and tensile property of a novel AlZnMgScZr alloy additively manufactured by gas atomization and laser powder bed fusion, Scr. Mater. 158 (2019) 24–28. https://doi.org/10.1016/j.scriptamat.2018.08.025.

[31] L. Zhou, H. Hyer, S. Thapliyal, R.S. Mishra, B. McWilliams, K. Cho, Y. Sohn, Process-Dependent Composition, Microstructure, and Printability of Al-Zn-Mg and Al-Zn-Mg-Sc-Zr Alloys Manufactured by Laser Powder Bed Fusion, Metall. Mater. Trans. A Phys. Metall. Mater. Sci. 51 (2020) 3215–3227. https://doi.org/10.1007/s11661-020-05768-3.

[32] P. Li, R. Li, H. Yang, T. Yuan, P. Niu, M. Wang, L. Li, C. Chen, Selective laser melting of Al-3.48Cu-2.03Si-0.48Sc-0.28Zr alloy: Microstructure evolution, properties and metallurgical defects, Intermetallics. 129 (2021) 107008. https://doi.org/10.1016/j.intermet.2020.107008.

[33] Z. Wang, X. Lin, N. Kang, J. Chen, Y. Tang, H. Tan, X. Yu, H. Yang, W. Huang, Directed energy deposition additive manufacturing of a Sc/Zr-modified Al–Mg alloy: Effect of thermal history on microstructural evolution and mechanical properties, Mater. Sci. Eng. A. 802 (2021) 140606. https://doi.org/10.1016/j.msea.2020.140606.

[34] P. Kürnsteiner, P. Bajaj, A. Gupta, M.B. Wilms, A. Weisheit, X. Li, C. Leinenbach, B. Gault, E.A. Jägle, D. Raabe, Control of thermally stable core-shell nano-precipitates in additively manufactured Al-Sc-Zr alloys, Addit. Manuf. 32 (2020) 100910. https://doi.org/10.1016/j.addma.2019.100910.

[35] Y. Shi, K. Yang, S.K. Kairy, F. Palm, X. Wu, P.A. Rometsch, Effect of platform temperature on the porosity, microstructure and mechanical properties of an Al–Mg–Sc–Zr alloy fabricated by selective laser melting, Mater. Sci. Eng. A. 732 (2018) 41–52. https://doi.org/10.1016/j.msea.2018.06.049.

[36] K. V. Yang, Y. Shi, F. Palm, X. Wu, P. Rometsch, Columnar to equiaxed transition in Al-Mg(-Sc)-Zr alloys produced by selective laser melting, Scr. Mater. 145 (2018) 113–117. https://doi.org/10.1016/j.scriptamat.2017.10.021.

[37] A.B. Spierings, K. Dawson, P.J. Uggowitzer, K. Wegener, Influence of SLM scan-speed on microstructure, precipitation of Al3Sc particles and mechanical properties in Sc- and Zr-modified Al-Mg alloys, Mater. Des. 140 (2018) 134–143. https://doi.org/10.1016/j.matdes.2017.11.053.

[38] S. Griffiths, M.D. Rossell, J. Croteau, N.Q. Vo, D.C. Dunand, C. Leinenbach, Effect of laser rescanning on the grain microstructure of a selective laser melted Al-Mg-Zr alloy, Mater. Charact. 143 (2018) 34–42. https://doi.org/10.1016/j.matchar.2018.03.033.

[39] E. Brandl, U. Heckenberger, V. Holzinger, D. Buchbinder, Additive manufactured AlSi10Mg samples using Selective Laser Melting (SLM): Microstructure, high cycle fatigue, and fracture behavior, Mater. Des. 34 (2012) 159–169. https://doi.org/10.1016/j.matdes.2011.07.067.

[40] M. Tang, P.C. Pistorius, Fatigue life prediction for AlSi10Mg components produced by selective laser melting, Int. J. Fatigue. 125 (2019) 479–490. https://doi.org/10.1016/j.ijfatigue.2019.04.015.

[41] Z.W. Xu, Q. Wang, X.S. Wang, C.H. Tan, M.H. Guo, P.B. Gao, High cycle fatigue performance of AlSi10mg alloy produced by selective laser melting, Mech. Mater. 148 (2020). https://doi.org/10.1016/j.mechmat.2020.103499.

[42] Z.K. Wu, S.C. Wu, J.G. Bao, W.J. Qian, S. Karabal, W. Sun, P.J. Withers, The effect of defect population on anisotropic fatigue resistance of selective laser melted AlSi10Mg alloy, Int. J. Fatigue. 151 (2021) 106317. https://doi.org/10.1016/j.ijfatigue.2021.106317.

[43] A.B. Spierings, K. Dawson, K. Kern, F. Palm, K. Wegener, SLM-processed Sc- and Zr- modified Al-Mg alloy: Mechanical properties and microstructural effects of heat treatment, Mater. Sci. Eng. A. 701 (2017) 264–273. https://doi.org/10.1016/j.msea.2017.06.089.

[44] L. Zhou, H. Hyer, S. Park, H. Pan, Y. Bai, K.P. Rice, Y. Sohn, Microstructure

and mechanical properties of Zr-modified aluminum alloy 5083 manufactured by laser powder bed fusion, Addit. Manuf. 28 (2019) 485–496. https://doi.org/10.1016/j.addma.2019.05.027.

[45] Standard Test Method for Analysis of Aluminum and Aluminum Alloys by Inductively Coupled Plasma Atomic Emission Spectrometry (Performance Based Method), Stand. Test Method Anal. Alum. Alum. Alloy. by Inductively Coupled Plasma At. Emiss. Spectrom. (Performance Based Method). 03.05 (2017). http://dx.doi.org/10.1520/E3061-17.

[46] Metal Material Axial Loading Fatigue Test Method，China National Standard GB/T 3075-2008, (n.d.).

[47] Metallic Materials-Tensile testing-Part 1: Method of test at room temperature，China National Standard GB/T 228.1-2010, (2010).

[48] A. du Plessis, I. Yadroitsava, I. Yadroitsev, Effects of defects on mechanical properties in metal additive manufacturing: A review focusing on X-ray tomography insights, Mater. Des. 187 (2020) 108385. https://doi.org/10.1016/j.matdes.2019.108385.

[49] N. Sanaei, A. Fatemi, Defects in Additive Manufactured Metals and Their Effect on Fatigue Performance: A State-of-the-Art Review, Prog. Mater. Sci. (2020) 100724. https://doi.org/10.1016/j.pmatsci.2020.100724.

[50] C. Galy, E. Le Guen, E. Lacoste, C. Arvieu, Main defects observed in aluminum alloy parts produced by SLM: From causes to consequences, Addit. Manuf. 22 (2018) 165–175. https://doi.org/10.1016/j.addma.2018.05.005.

[51] S. Afkhami, M. Dabiri, S.H. Alavi, T. Björk, A. Salminen, Fatigue characteristics of steels manufactured by selective laser melting, Int. J. Fatigue. 122 (2019) 72–83. https://doi.org/10.1016/j.ijfatigue.2018.12.029.

[52] P. Kumar, U. Ramamurty, High cycle fatigue in selective laser melted Ti-6Al-4V, Acta Mater. 194 (2020) 305–320. https://doi.org/10.1016/j.actamat.2020.05.041.

[53] C. Xie, S. Wu, Y. Yu, H. Zhang, Y. Hu, M. Zhang, G. Wang, Defect-correlated fatigue resistance of additively manufactured Al-Mg4.5Mn alloy with in situ

micro-rolling, J. Mater. Process. Technol. 291 (2021) 117039. https://doi.org/10.1016/j.jmatprotec.2020.117039.

[54] P. Wang, H. Lei, X. Zhu, H. Chen, D. Fang, Influence of manufacturing geometric defects on the mechanical properties of AlSi10Mg alloy fabricated by selective laser melting, J. Alloys Compd. 789 (2019) 852–859. https://doi.org/10.1016/j.jallcom.2019.03.135.

[55] A.R. Balachandramurthi, J. Moverare, N. Dixit, R. Pederson, Influence of defects and as-built surface roughness on fatigue properties of additively manufactured Alloy 718, Mater. Sci. Eng. A. 735 (2018) 463–474. https://doi.org/10.1016/j.msea.2018.08.072.

[56] A.B. Spierings, K. Dawson, P. Dumitraschkewitz, S. Pogatscher, K. Wegener, Microstructure characterization of SLM-processed Al-Mg-Sc-Zr alloy in the heat treated and HIPed condition, Addit. Manuf. 20 (2018) 173–181. https://doi.org/10.1016/j.addma.2017.12.011.

[57] Z. Wang, X. Lin, Y. Tang, N. Kang, X. Gao, S. Shi, W. Huang, Laser-based directed energy deposition of novel Sc/Zr-modified Al-Mg alloys: columnar-to-equiaxed transition and aging hardening behavior, J. Mater. Sci. Technol. 69 (2021) 168–179. https://doi.org/10.1016/j.jmst.2020.08.003.

[58] X. Gao, Y. Wu, C. Hutchinson, Training high-strength aluminum alloys to withstand fatigue, Nat. Commun. (n.d.) 1–8. https://doi.org/10.1038/s41467-020-19071-7.

[59] R. Liu, Y. Tian, Z. Zhang, X. An, P. Zhang, Z. Zhang, Exceptional high fatigue strength in Cu-15at.%Al alloy with moderate grain size, Sci. Rep. 6 (2016) 1–9. https://doi.org/10.1038/srep27433.

[60] Z.W. Xu, A. Liu, X.S. Wang, The influence of building direction on the fatigue crack propagation behavior of Ti6Al4V alloy produced by selective laser melting, Mater. Sci. Eng. A. 767 (2019). https://doi.org/10.1016/j.msea.2019.138409.

[61] K. Schmidtke, F. Palm, A. Hawkins, C. Emmelmann, Process and mechanical properties: Applicability of a scandium modified Al-alloy for laser additive

manufacturing, Phys. Procedia. 12 (2011) 369–374. https://doi.org/10.1016/j.phpro.2011.03.047.

[62] H. Li, S. Gao, Y. Tomota, S. Ii, N. Tsuji, T. Ohmura, Mechanical response of dislocation interaction with grain boundary in ultrafine-grained interstitial-free steel, Acta Mater. 206 (2021) 116621. https://doi.org/10.1016/j.actamat.2021.116621.

[63] O. Basquin, The exponential law of endurance tests, Proc ASTM. 10 (1910).

[64] W.J. Dixon, A.M. Mood, A Method for Obtaining and Analyzing Sensitivity Data, J. Am. Stat. Assoc. 43 (1948) 109–126. https://doi.org/10.1080/01621459.1948.10483254.

[65] T.. H.. Smith , K . N ., Watson , P . and Topper, A StressStrain Function for the Fatigue of Metals, 5 (2017).

[66] M. Besel, Y. Besel, U. Alfaro Mercado, T. Kakiuchi, Y. Uematsu, Fatigue behavior of friction stir welded Al-Mg-Sc alloy, Int. J. Fatigue. 77 (2015) 1–11. https://doi.org/10.1016/j.ijfatigue.2015.02.013.

[67] Y. Estrin, A. Vinogradov, Fatigue behaviour of light alloys with ultrafine grain structure produced by severe plastic deformation: An overview, Int. J. Fatigue. 32 (2010) 898–907. https://doi.org/10.1016/j.ijfatigue.2009.06.022.

[68] A. Vinogradov, A. Washikita, K. Kitagawa, V.I. Kopylov, Fatigue life of fine-grain Al-Mg-Sc alloys produced by equal-channel angular pressing, Mater. Sci. Eng. A. 349 (2003) 318–326. https://doi.org/10.1016/S0921-5093(02)00813-4.

[69] H. Gong, K. Rafi, H. Gu, G.D. Janaki Ram, T. Starr, B. Stucker, Influence of defects on mechanical properties of Ti-6Al-4V components produced by selective laser melting and electron beam melting, Mater. Des. 86 (2015) 545–554. https://doi.org/10.1016/j.matdes.2015.07.147.

[70] X.F. Ma, H.L. Zhai, L. Zuo, W.J. Zhang, S.S. Rui, Q.N. Han, J.S. Jiang, C.P. Li, G.F. Chen, G.A. Qian, S.J. Zhao, Fatigue short crack propagation behavior of selective laser melted Inconel 718 alloy by in-situ SEM study: Influence of orientation and temperature, Int. J. Fatigue. 139 (2020). https://doi.org/10.1016/j.ijfatigue.2020.105739.

[71] H. Zhang, M. Xu, Z. Liu, C. Li, P. Kumar, Z. Liu, Y. Zhang, Microstructure, surface quality, residual stress, fatigue behavior and damage mechanisms of selective laser melted 304L stainless steel considering building direction, Addit. Manuf. (2021) 102147. https://doi.org/10.1016/j.addma.2021.102147.

[72] A. Ramanathan, J. Moverare, T. Hansson, R. Pederson, Anisotropic fatigue properties of Alloy 718 manufactured by Electron Beam Powder Bed Fusion, Int. J. Fatigue. 141 (2020) 105898. https://doi.org/10.1016/j.ijfatigue.2020.105898.

[73] Y. Murakami, H. Masuo, Y. Tanaka, M. Nakatani, Defect Analysis for Additively Manufactured Materials in Fatigue from the Viewpoint of Quality Control and Statistics of Extremes, Procedia Struct. Integr. 19 (2019) 113–122. https://doi.org/10.1016/j.prostr.2019.12.014.

[74] R. Biswal, A.K. Syed, X. Zhang, Assessment of the effect of isolated porosity defects on the fatigue performance of additive manufactured titanium alloy, Addit. Manuf. 23 (2018) 433–442. https://doi.org/10.1016/j.addma.2018.08.024.

[75] S. Kitagawa, H., Takahashi, Application of fracture mechanics to very small cracks or the cracks in early stage, Proc. 2nd ICM, Clevel. p.627 (1976) 627–631. https://ci.nii.ac.jp/naid/10025887201%0Ahttps://ci.nii.ac.jp/naid/10025887201/.

[76] Manuscript-R2, (n.d.).

[77] C. Watanabe, R. Monzen, K. Tazaki, Effects of Al3Sc particle size and precipitate-free zones on fatigue behavior and dislocation structure of an aged Al-Mg-Sc alloy, Int. J. Fatigue. 30 (2008) 635–641. https://doi.org/10.1016/j.ijfatigue.2007.05.010.

[78] V. Gerold, H.P. Karnthaler, On the origin of planar slip in f.c.c. alloys, Acta Metall. 37 (1989) 2177–2183. https://doi.org/10.1016/0001-6160(89)90143-0.

[79] C. Watanabe, C.Y. Jin, R. Monzen, K. Kitagawa, Low-cycle fatigue behavior and dislocation structure of an Al-Mg-Sc alloy, Mater. Sci. Eng. A. 387–389

(2004) 552–555. https://doi.org/10.1016/j.msea.2004.05.079.

[80] T. Zhai, A.J. Wilkinson, J.W. Martin, Crystallographic mechanism for fatigue crack propagation through grain boundaries, Acta Mater. 48 (2000) 4917–4927. https://doi.org/10.1016/S1359-6454(00)00214-7.

[81] A.R. Balachandramurthi, J. Moverare, N. Dixit, D. Deng, R. Pederson, Microstructural influence on fatigue crack propagation during high cycle fatigue testing of additively manufactured Alloy 718, Mater. Charact. 149 (2019) 82–94. https://doi.org/10.1016/j.matchar.2019.01.018.

[82] G. Liu, S. Winwood, K. Rhodes, S. Birosca, The effects of grain size, dendritic structure and crystallographic orientation on fatigue crack propagation in IN713C nickel-based superalloy, Int. J. Plast. 125 (2020) 150–168. https://doi.org/10.1016/j.ijplas.2019.09.010.

[83] N. Kumar, R.S. Mishra, C.S. Huskamp, K.K. Sankaran, Critical grain size for change in deformation behavior in ultrafine grained Al-Mg-Sc alloy, Scr. Mater. 64 (2011) 576–579. https://doi.org/10.1016/j.scriptamat.2010.11.051.

[84] P.L. Sun, C.Y. Yu, P.W. Kao, C.P. Chang, Influence of boundary characters on the tensile behavior of sub-micron-grained aluminum, Scr. Mater. 52 (2005) 265–269. https://doi.org/10.1016/j.scriptamat.2004.10.022.

[85] R.W. Hayes, D. Witkin, F. Zhou, E.J. Lavernia, Deformation and activation volumes of cryomilled ultrafine-grained aluminum, Acta Mater. 52 (2004) 4259–4271. https://doi.org/10.1016/j.actamat.2004.05.042.

[86] R. Kapoor, J.B. Singh, J.K. Chakravartty, High strain rate behavior of ultrafine-grained Al-1.5 Mg, Mater. Sci. Eng. A. 496 (2008) 308–315. https://doi.org/10.1016/j.msea.2008.05.043.

[87] N. Kumar, R.S. Mishra, Additivity of strengthening mechanisms in ultrafine grained Al-Mg-Sc alloy, Mater. Sci. Eng. A. 580 (2013) 175–183. https://doi.org/10.1016/j.msea.2013.05.006.

[88] V. Yamakov, D. Wolf, S.R. Phillpot, A.K. Mukherjee, H. Gleiter, Dislocation processes in the deformation of nanocrystalline aluminium by molecular-dynamics simulation, Nat. Mater. 1 (2002) 45–48.

https://doi.org/10.1038/nmat700.